IMMUNOLOGY

Stiffness sensing via Piezo1 enhances macrophage efferocytosis and promotes the resolution of liver fibrosis

Yang Wang[1]†, Jin Wang[1]†, Jiahao Zhang[1]†, Yina Wang[1], Yuanyuan Wang[1], Haixia Kang[1], Wenying Zhao[1], Wenjuan Bai[1], Naijun Miao[1], Jing Wang[1,2]*

Copyright © 2024 The Authors, some rights reserved; exclusive licensee American Association for the Advancement of Science. No claim to original U.S. Government Works. Distributed under a Creative Commons Attribution NonCommercial License 4.0 (CC BY-NC).

Tissue stiffening is a predominant feature of fibrotic disorders, but the response of macrophages to changes in tissue stiffness and cellular context in fibrotic diseases remains unclear. Here, we found that the mechanosensitive ion channel Piezo1 was up-regulated in hepatic fibrosis. Macrophages lacking Piezo1 showed sustained inflammation and impaired spontaneous resolution of early liver fibrosis. Further analysis revealed an impairment of clearance of apoptotic cells by macrophages in the fibrotic liver. Macrophages showed enhanced efferocytosis when cultured on rigid substrates but not soft ones, suggesting stiffness-dependent efferocytosis of macrophages required Piezo1 activation. Besides, Piezo1 was involved in the efficient acidification of the engulfed cargo in the phagolysosomes and affected the subsequent expression of anti-inflammation genes after efferocytosis. Pharmacological activation of Piezo1 increased the efferocytosis capacity of macrophages and accelerated the resolution of inflammation and fibrosis. Our study supports the antifibrotic role of Piezo1-mediated mechanical sensation in liver fibrosis, suggesting that targeting PIEZO1 to enhance macrophage efferocytosis could induce fibrosis regression.

INTRODUCTION

Liver cirrhosis is a major cause of morbidity and mortality worldwide and has limited therapeutic options. Fibrosis is a characteristic feature of chronic liver disease regardless of the etiology (*1*). It is now understood that liver fibrosis arises from various insults that lead to liver injury, triggering a wound-healing response. With repeated and chronic injury, the normal wound healing response becomes aberrant, leading to hepatic stellate cell (HSC) activation, extracellular matrix (ECM) deposition, tissue remodeling, and subsequent tissue stiffening. The increased stiffness of the liver has been correlated with fibrosis progression (*2*). Several cell types have been reported to be involved in sensing the change in mechanical properties. Myofibroblasts transdifferentiated from HSCs are the major source of ECM production and contribute to hepatic fibrosis. A stiff environment alone can promote myofibroblastic activation of HSCs (*3*). This feed-forward loop between HSC activation and tissue stiffening may further enhance fibrogenesis. Sinusoid angiogenesis has been established as a hallmark of liver fibrogenesis. Liver sinusoid endothelial cells plated on a soft substrate (140 to 610 Pa) formed capillary-like structures, simulating angiogenesis during the early stage of liver fibrosis in contrast with a hard substrate (>1.2 kPa) (*4*). Despite the growing understanding of the mechanical properties in mediating fibrosis, how immune cells are regulated by mechanical signals during liver fibrosis remains largely unexplored.

Macrophages have long been considered to be key drivers of fibrogenesis (*5*). However, several recent studies have revealed the complex and often paradoxical role of macrophages in regulating liver fibrosis (*6*, *7*). It is well recognized that macrophages exhibit either pro- or antifibrotic functions during tissue repair since macrophages are heterogeneous populations with considerable plasticity (*8*). There are at least two subsets of hepatic macrophages, the liver resident macrophages (Kupffer cells) and recruited monocyte-derived macrophages (MoDMs). During the early stages of liver injury, Kupffer cells are activated by damage-associated molecular patterns released from dead hepatocytes and release cytokines or chemokines that further recruit circulating monocytes (*9*). Ly6c^{high} monocytes are recruited during the progression of liver injury and gradually converted into Ly6c^{low} macrophages. The Ly6c^{low} macrophages display a restorative phenotype that can promote fibrosis resolution (*6*). Many pro- or antifibrotic effectors secreted from these subsets have been studied intensively, but the mechanisms underlying the regulation of these functions remain largely unknown. In addition, the function of macrophages is highly regulated by tissue environmental cues such as tissue localization, neighboring cells, and the mechanical properties of the tissue. Although it has been shown that macrophages cultured on a rigid substrate are more prone to pro-inflammatory phenotype (*10*, *11*), how changes in mechanical properties regulate different macrophages in the context of liver fibrosis remains elusive. Piezo1 is a mechanical-sensitive ion channel protein crucial in various pathophysiological processes (*12*). Previous studies have demonstrated that myeloid-specific depletion of Piezo1-protected mice against pulmonary fibrosis and renal fibrosis (*13*, *14*). In both studies, Piezo1 activation by cyclic stretch enhanced the expression of pro-inflammatory cytokines and chemokines in macrophages. Nonetheless, whether piezo1-mediated stiffness sensing by macrophages also contributes to liver fibrotic disease remains unclear.

In this study, we sought to explore the role of mechanical signals in regulating macrophage response during liver fibrosis. We found that Piezo1 was highly expressed in both human and murine fibrotic liver, and mice lacking piezo1 in macrophages exhibited more severe liver inflammation and fibrosis due to the impaired clearance of apoptotic cells. Using an in vitro culture system that mimics the stiffness of a fibrotic liver, we revealed the protective role of piezo1 in promoting phagocytosis and clearance of apoptotic cells by macrophages, a

[1]Shanghai Institute of Immunology, Department of Immunology and Microbiology, Shanghai Jiao Tong University School of Medicine, Shanghai 200025, China. [2]Center for Immune-related Diseases at Shanghai Institute of Immunology, Ruijin Hospital, Shanghai Jiao Tong University School of Medicine, Shanghai, China.
*Corresponding author. Email: jingwang@shsmu.edu.cn
†These authors contributed equally to this work.

process known as efferocytosis. Besides, Piezo1 could promote the acidification and digestion of apoptotic cargo in phagosomes. Subsequently, Piezo1-dependent efferocytosis limited the expression of pro-inflammatory signatures and converted macrophages into anti-inflammatory phenotype. Systemic administration of the Piezo1-specific agonist, Yoda1, accelerated the resolution of inflammation and fibrosis, suggesting that Piezo1 may be a potential therapeutic target for fibrosis treatment.

RESULTS

Disease-associated up-regulation of piezo1 in liver macrophages

To investigate the association between PIEZO1 and liver fibrosis, we first performed an analysis with public repositories of transcription profiling datasets of the liver from patients with various stages of nonalcoholic fatty liver disease. We found that PIEZO1 positively correlated with genes encoding collagens such as COL1A1, COL3A1, and COL6A1 (Fig. 1, A to C) (*15*). Gene Ontology (GO) enrichment analysis of genes showed a positive correlation with PIEZO1, suggesting that these genes were linked to biological processes, including regulation of cell morphogenesis, guanosine triphosphatase (GTPase) activity, actin cytoskeleton organization, cell-substrate junction assembly, cellular response to growth factor stimulus, and ECM organization (Fig. 1D). Meanwhile, genes negatively correlated with PIEZO1 were mostly linked to biological functions of the liver, such as the metabolism of protein, peptides, vitamins, cofactors, fatty acids, and the tricarboxylic acid cycle (fig. S1A). Analysis of public repositories of transcription profiling datasets of mice liver revealed an increased Piezo1 expression with nonalcoholic fatty liver disease (NASH, nonalcoholic steatohepatitis) disease modeling (Fig. 1E) (GSE83596).

Previous studies have reported the expression of Piezo1 in bone marrow–derived macrophages (BMDMs) and liver resident Kupffer cells (KCs) (*13*, *16*). To validate whether Piezo1 was up-regulated in liver macrophages during fibrosis, we analyzed the levels of transcripts of Piezo1 in liver macrophages using published transcriptomic profiling data of mice liver macrophages. We found up-regulated expression of Piezo1 in KCs with the development of the NASH disease model (Fig. 1F) (*17*). Furthermore, circulating monocytes can infiltrate the liver and undergo differentiation into macrophages. Notably, these macrophages can be classified into two distinct populations based on the expression of Ly6c. We found that compared with the other subpopulations of liver macrophages, Ly6c^{lo} and Ly6c^{hi} recruited macrophages expressed higher levels of Piezo1 transcripts (Fig. 1G).

To determine the expression of Piezo1 in liver macrophage during fibrosis, we next used a liver fibrosis mice model in which chronic liver injury was induced by repeated intraperitoneal injection of carbon tetrachloride (CCl4). Using flow cytometry, we successfully identified three heterogeneous populations of liver macrophages during CCl4-induced liver fibrosis, including CD11b^{lo} CD64^{hi} F4/80^{hi} KCs, CD11b^{hi} CD64^{lo} F4/80^{lo} Ly6c^{lo} monocyte-derived macrophages (Ly6c^{lo} MoDMs), and CD11b^{hi} CD64^{lo} F4/80^{lo} Ly6c^{hi} monocyte-derived macrophages (Ly6c^{hi} MoDMs) (fig. S1B). We also performed quantitative polymerase chain reaction (qPCR) analysis of several sorted myeloid cell populations to measure the mRNA level of Piezo1 and found that Ly6c^{lo} MoDM had the highest Piezo1 mRNA expression level (fig. S1C). To confirm the protein level of Piezo1 expression, we induced liver fibrosis in Piezo1^{P1tdT} transgenic mice, in which Piezo1 was tagged with the fluorescent protein tdTomato. By comparing the mean fluorescence intensity (MFI) of tdTomato with wild-type (WT) control mice, we found that Piezo1 expressed in all three liver macrophage populations and hepatic sinusoidal endothelial cells (HSECs). Piezo1 was also detected in neutrophils and eosinophils with relatively lower expression. Besides, the expression of Piezo1 was up-regulated during CCl4-induced chronic liver injury in HSECs, KCs, and Ly6chi MoDMs (Fig. 1H). Liver fibrosis caused a prominent accumulation of macrophages and neutrophils in the fibrotic region, defined by enriched a-SMA^{+} myofibroblasts area (fig. S1D). Consistent with the result of flow cytometry, immunofluorescent staining revealed that Piezo1 was colocalized with F4/80^{+} macrophages and was significantly up-regulated during chronic liver injury. Besides, macrophages in the fibrotic region showed the highest Piezo1 expression (Fig. 1, I and J). Therefore, these data suggested a strong correlation between Piezo1 expression and liver fibrosis in humans and mice and up-regulation of Piezo1 in liver macrophages, indicating Piezo1 may play an essential role in liver fibrosis.

Myeloid-specific Piezo1 deficiency exacerbates liver fibrosis

To explore the role of macrophage Piezo1 in liver fibrosis, we generated Piezo1$^{fl/fl}$ Lyz2^{Cre} mice to specifically deplete Piezo1 in myeloid cells and induced liver fibrosis in these mice and their littermate controls (Piezo1$^{fl/fl}$ mice) by eight injections of CCl_4. Sirius red staining showed that the fibrotic area in Piezo1$^{fl/fl}$ Lyz2^{Cre} mice was comparable with Piezo1$^{fl/fl}$ mice 24 hours after the last CCl_4 injection. However, Piezo1$^{fl/fl}$ Lyz2^{Cre} mice displayed significantly increased fibrotic area 48 hours after the last CCl_4 injection (Fig. 2, A to C). Similarly, after the last CCl_4 injection, immunofluorescent staining of α–smooth muscle actin (α-SMA) showed an increased α-SMA–positive area in Piezo1$^{fl/fl}$ Lyz2^{Cre} mice at 48 hours but not at 24 hours (Fig. 2, D to F). Besides, mRNA levels of fibrosis-related genes, including α-SMA, Timp1, Col1a1, Col3a1, and Col6a1, were also increased in the liver from Piezo1$^{fl/fl}$ Lyz2^{Cre} mice at 48 hours but not at 24 hours (Fig. 2, G and H). Piezo1 conditional knockout in myeloid cells also resulted in higher serum alanine aminotransferase (ALT) and aspartate aminotransferase (AST) levels at both 24 and 48 hours (Fig. 2, I to L). Unexpectedly, there was no difference between the level of serum ALT and AST in Piezo1$^{fl/fl}$ Lyz2^{Cre} mice and their littermate controls after an acute liver injury induced by one single dose of CCl_4 injection (fig. S2, A and B). We also used another liver fibrosis model induced by a high-fat choline-deficient, L-amino acid–defined (CDAHFD) diet (*18*). Similarly, serum ALT and AST were higher in Piezo1$^{fl/fl}$ Lyz2^{Cre} compared to their littermate control (Fig. 2, M and N). mRNA levels of fibrosis-related genes were also increased in Piezo1$^{fl/fl}$ Lyz2^{Cre} mice (Fig. 2O). Sirius red staining also revealed more fibrosis in the liver from Piezo1$^{fl/fl}$ Lyz2^{Cre} mice (Fig. 2, P and Q). These data suggest that Piezo1 in liver macrophages contributes to the resolution of liver injury and fibrosis during chronic liver disease.

Piezo1 deficiency is related to impaired efferocytosis function in fibrotic mice

To further elucidate how myeloid-specific depletion of Piezo1 affects the resolution of chronic liver injury and fibrosis, we assessed the proportion of major myeloid cells in the liver using flow cytometry. Neutrophils, but not macrophages, showed an increased abundance at 24 and 48 hours after the last CCl_4 injection (Fig. 3, A to D, and fig. S3, A and B), which was validated by immunofluorescent staining (Fig. 3, E to G). The proportion and absolute count of neutrophils

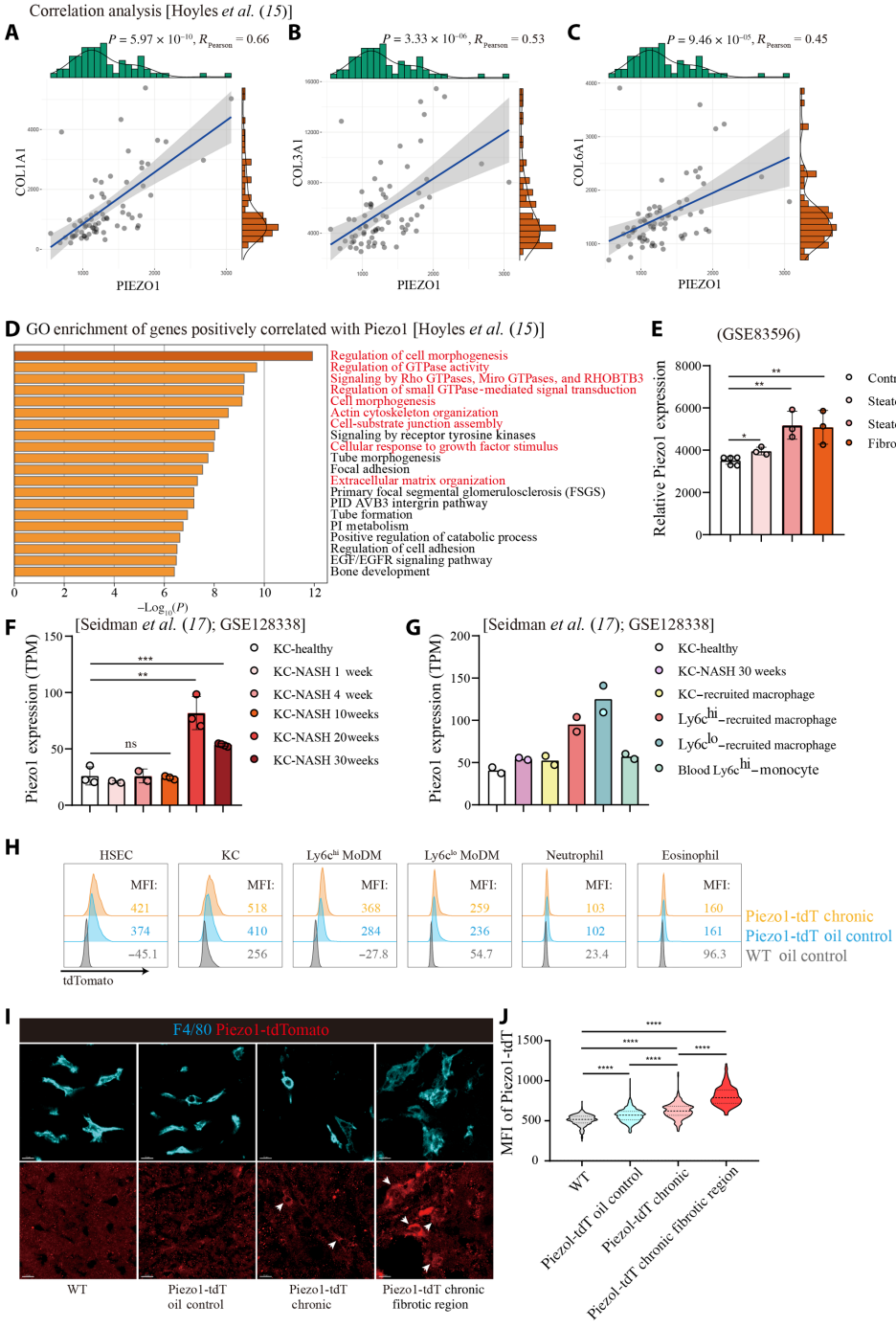

Fig. 1. Increased expression of Piezo1 in liver macrophages during the progression of NASH. (**A** to **C**) Correlation analysis of PIEZO1 with COL1A1 (A), COL3A1 (B), and COL6A1 (C) using human transcription profiling dataset from public data. Every spot represents an individual patient. The *P* values and correlation coefficients were calculated using Pearson's correlation analysis. (**D**) Biofunction analysis of top 100 genes positively correlated with PIEZO1 in human transcription profiling dataset. Pathways mentioned in the text are highlighted. (**E**) Normalized Piezo1 expression in mice liver during NASH progression analyzed by transcription profiling dataset from public data. Each spot represents a biological duplication of samples. (**F** and **G**) Normalized Piezo1 expression in Kupffer cells (F) and different monocyte or macrophage subpopulations (G) during NASH progression analyzed by transcription profiling dataset from public datasets. Each spot represents a biological duplication of samples (E to G). (**H**) Histogram plots of tdTomato intensities of HSECs, KCs, Ly6c^{hi} MoDMs, Ly6c^{lo} MoDMs, neutrophils, and eosinophils measured by flow cytometry. The mean fluorescence intensity (MFI) of cells from wild-type mice liver (WT oil control), Piezo1^{P1tdT} mice liver treated with corn oil (Piezo1-tdT oil control) or repetitive CCl_4 challenge (Piezo1-tdT chronic) was shown in the corresponding colors. (**I**) Representative confocal images of liver sections showing tdTomato (red) expression in F4/80-positive (cyan) liver macrophages in WT mice, Piezo1-tdT oil control mice, normal region, and fibrotic region of Piezo1-tdT oil control mice. Scale bars, 10 μm. (**J**) Quantification of tdTomato expression in liver macrophages in (I). Data are displayed as means ± SD. Unpaired Student's two-tailed *t* test (E and F). One-way analysis of variance (ANOVA) with Tukey's multiple comparisons test (J). ns, nonsignificant, **P* < 0.05, ***P* < 0.01, ****P* < 0.001, and *****P* < 0.0001. Data are representative of two independent experiments (I and J).

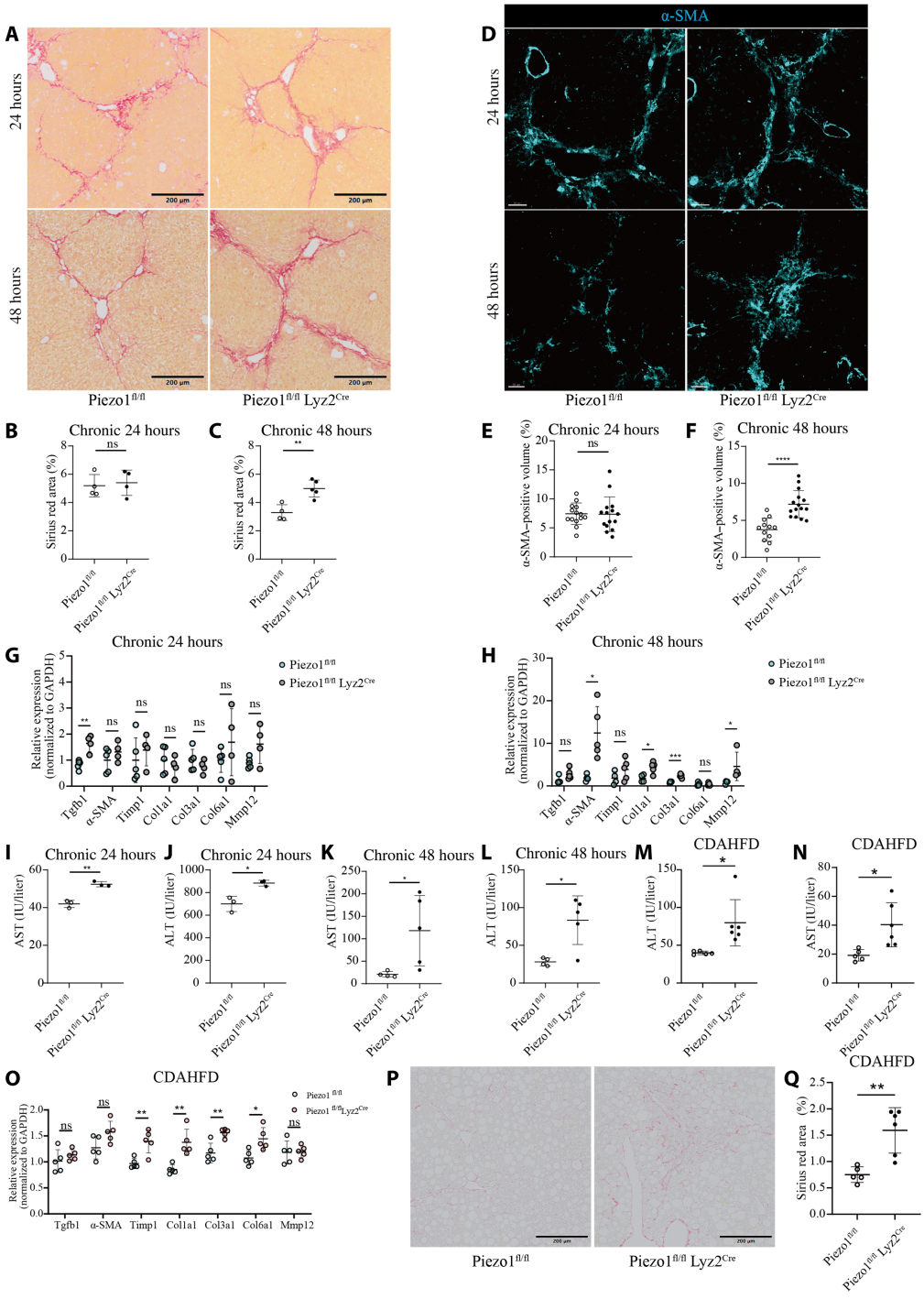

Fig. 2. Macrophage piezo1 knockout exacerbates liver fibrosis. (**A** to **C**) Representative image of Sirius red staining of the liver sections (A) and their quantifications of Piezo1$^{fl/fl}$ Lyz2^{Cre} mice and their littermate controls at 24 (B) and 48 hours (C) after the last injection of CCl_4. Scale bars, 200 μm. $n = 3$ to 5 mice. (**D** to **F**) Representative immunofluorescence staining image of α–smooth muscle actin (α-SMA) of the liver sections (D) and their quantifications of Piezo1$^{fl/fl}$ Lyz2^{Cre} mice and their littermate controls at 24 (E) and 48 hours (F) after chronic CCl_4 injury. Scale bars, 50 μm. Each dot represents one region of interest (ROI). (**G** and **H**) qPCR analysis of mRNA level of fibrosis-related genes in the liver of Piezo1$^{fl/fl}$ Lyz2^{Cre} mice and their littermate controls at the time point of 24 (G) and 48 hours (H) after chronic CCl_4 injury. $n = 3$ to 5 mice. (**I** to **L**) Quantification of serum alanine aminotransferase (ALT) and aspartate aminotransferase (AST) levels of Piezo1$^{fl/fl}$ Lyz2^{Cre} mice and their littermate controls at 24 (I and J) and 48 hours (K and L) after chronic CCl_4 injury. $n = 3$ to 5 mice. (**M** and **N**) Quantification of serum ALT (C) and AST (D) levels of Piezo1$^{fl/fl}$ Lyz2^{Cre} mice and their littermate controls fed with choline-deficient, L-amino acid–defined (CDAHFD) diet for 6 weeks. $n = 5$ mice per group. (**O**) qPCR analysis of mRNA level of fibrosis-related genes in the liver. $n = 5$ mice per group. (**P** and **Q**) Sirius red staining of the liver sections (P) and their quantifications (Q). $n = 5$ mice per group. Data are displayed as means ± SD. Unpaired Student's two-tailed *t* test (B, C, E, F, I to N, and Q). Two-way ANOVA with multiple comparisons test (G, H, and O). $^*P < 0.05$, $^{**}P < 0.01$, $^{***}P < 0.001$, and $^{****}P < 0.0001$. Data are representative of three independent experiments.

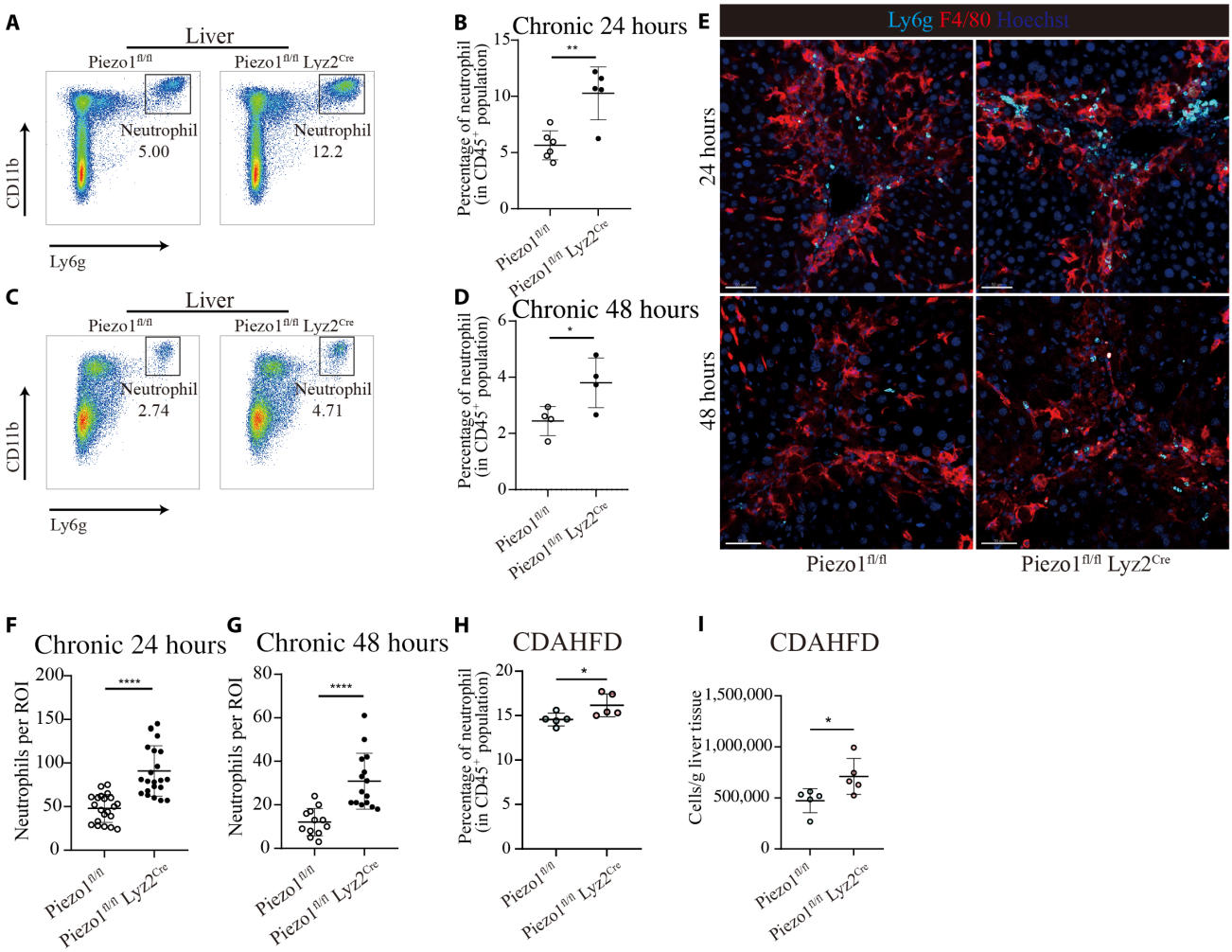

Fig. 3. Piezo1 deficiency resulted in more neutrophil accumulation in fibrotic mice. (**A** to **D**) Representative fluorescence-activated cell sorting (FACS) plot of neutrophil subsets and statistics of their frequencies in the liver of Piezo1$^{fl/fl}$ Lyz2^{Cre} mice and their littermate controls at 24 (A and B) and 48 hours (C and D) after chronic CCl_4 injury. After gating for CD45$^+$ living singlets, neutrophils were defined as CD11b$^+$ Ly6g$^+$ cells. $n = 4$ to 6 mice per group (B and D). (**E** to **G**) Representative immunofluorescence staining image of neutrophils (Ly6g, cyan) of the liver sections (E) and their quantifications of Piezo1$^{fl/fl}$ Lyz2^{Cre} mice and their littermate controls at 24 (F) and 48 hours (G) after chronic CCl_4 injury. Liver macrophages were visualized by F4/80 (red), and the nucleus was stained by Hoechst (blue). Scale bars, 50 μm. Each dot represents one ROI. (**H** and **I**) Frequency and numbers of neutrophils in the liver of Piezo1$^{fl/fl}$ Lyz2^{Cre} mice and their littermate controls after 6-week CDHFAA diet. $n = 5$ mice per group. Data are displayed as means ± SD. Unpaired Student's two-tailed *t* test (B, D, and F to I). *$P < 0.05$, **$P < 0.01$, and ****$P < 0.0001$. Data are representative of three independent experiments.

were also higher in CDAHFD-fed Piezo1$^{fl/fl}$ Lyz2^{Cre} mice compared to the littermate control (Fig. 3, H and I). Considering the low expression of Piezo1 in neutrophils within the liver (Fig. 1H), we did not attribute the observed effects on neutrophils to the impact of myeloid Piezo1 knockout. In addition, the number of neutrophils infiltrating the liver after acute injury was not changed (fig. S2, A and B), indicating that the activation signals derived from sensing damaged tissue may not contribute to Piezo1 activation. Besides, the neutrophil abundance in the bone marrow and blood was comparable between Piezo1$^{fl/fl}$ Lyz2^{Cre} mice and Piezo1$^{fl/fl}$ mice at both 24 and 48 hours after chronic liver injury (fig. S3, C to F), which suggested that Piezo1 knockout was unlikely to cause a difference in neutrophil recruitment during inflammation.

In the liver, apoptotic neutrophils are widely thought to be cleared by KCs via efferocytosis (*19*, *20*). Failure to clear apoptotic neutrophils during alcoholic liver disease can result in increased liver injury (*21*). Here, we hypothesized that myeloid depletion of Piezo1 impairs the efferocytosis of neutrophils by liver macrophages. To confirm whether this clearance program also occurs in CCl_4-induced chronic liver injury, we first used immunofluorescence to assess the colocalization of neutrophils and macrophages. We observed neutrophils were localized in the cell body of macrophages during chronic liver injury, especially in the fibrotic region (Fig. 4, A and B). In the fibrotic region of Piezo1$^{fl/fl}$ mice, we observed a higher proportion of neutrophils that were localized within macrophages, despite the lower overall abundance of neutrophils, compared to Piezo1$^{fl/fl}$ Lyz2^{Cre} mice (Fig. 4, C and D), indicating that macrophages engulfed fewer neutrophils in Piezo1$^{fl/fl}$ Lyz2^{Cre} mice. To determine the contribution of KCs, Ly6c^{lo} MoDMs, and Ly6c^{hi} MoDMs to neutrophil efferocytosis during chronic liver fibrosis, we developed a gating strategy using flow cytometry to identify engulfing macrophages by intracellular staining of Ly6g (Fig. 4,

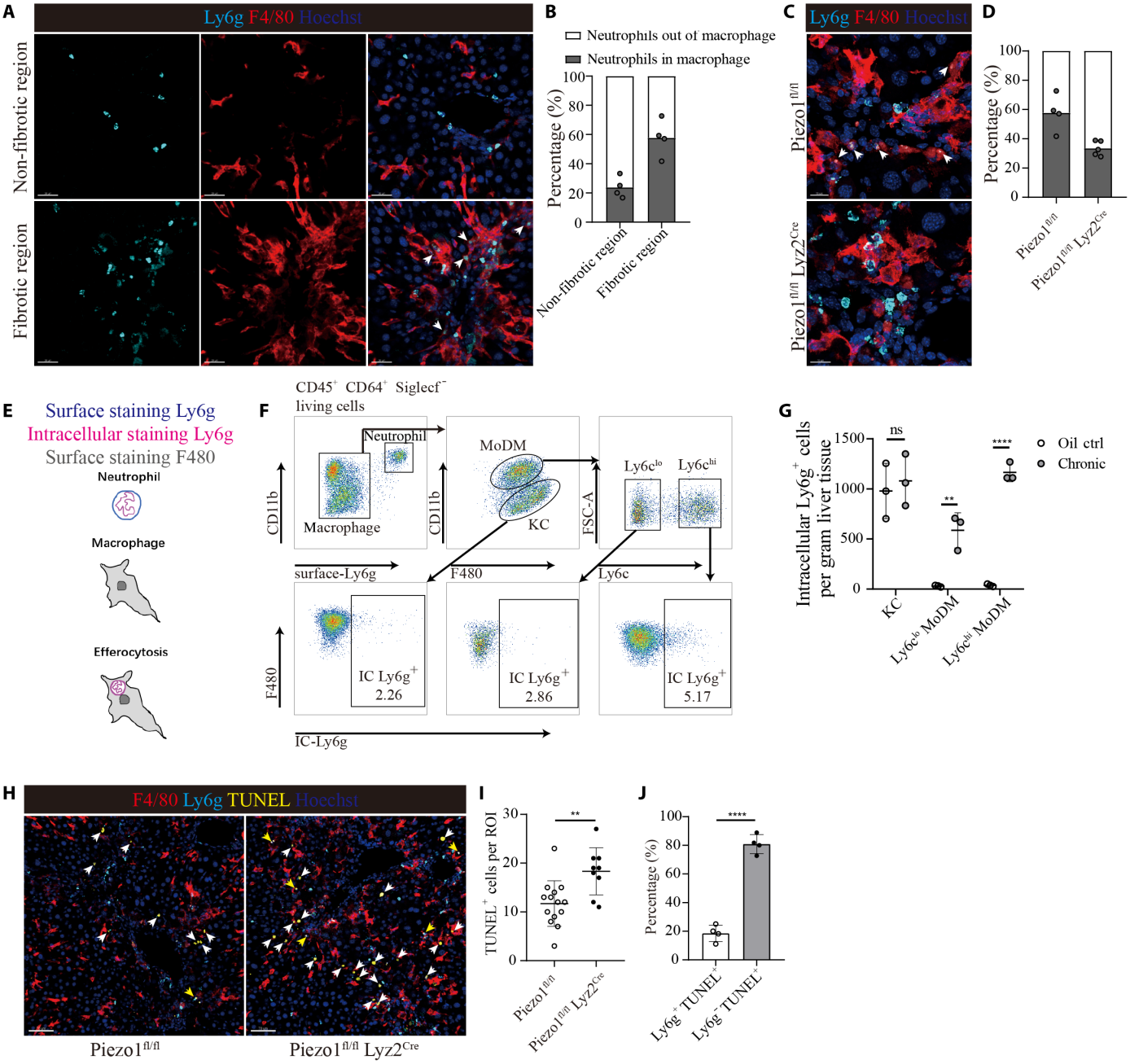

Fig. 4. Piezo1 deficiency impaired efferocytosis of macrophages in fibrotic mice. (**A** and **B**) Representative confocal image of immunofluorescence staining showing the colocalization of neutrophils (Ly6g, cyan) and liver macrophages (F4/80, red) in the non-fibrotic region and fibrotic region; the nucleus was stained by Hoechst (blue) (A). Neutrophils localized in macrophages were indicated with white arrows. Scale bars, 30 μm. The percentage of neutrophils localized in macrophages was quantified as in (B). $n = 4$ mice per group. (**C** and **D**) Representative confocal image of immunofluorescence staining (C) and their quantifications (D) showing the colocalization of neutrophils (Ly6g, cyan) and liver macrophages (F4/80, red) in the fibrotic region of Piezo1$^{fl/fl}$ Lyz2^{Cre} mice liver and their littermate controls. Neutrophils localized in macrophages were indicated with white arrows. Scale bars, 15 μm. $n = 4$ mice per group. (**E**) Experimental scheme for the identification of neutrophil-engulfing liver macrophages. (**F**) Representative FACS plot for the identification of neutrophil-engulfing liver macrophages. (**G**) Absolute cell numbers of neutrophil-engulfing liver macrophages of control mice treated with corn oil vehicle or chronic CCl_4 injury mice. (**H** and **I**) Representative confocal image of terminal deoxynucleotidyl transferase–mediated deoxyuridine triphosphate nick end labeling (TUNEL; yellow) staining of liver sections (H) and their quantifications (I) of Piezo1$^{fl/fl}$ Lyz2^{Cre} mice and their littermate controls at 24 hours after chronic CCl_4 injury. Liver macrophages were visualized by F4/80 (red), neutrophils were visualized by Ly6g (cyan), and the nucleus was stained by Hoechst (blue). Scale bars, 70 μm. Each dot represents one ROI. (**J**) Percentage of Ly6g-positive or -negative, TUNEL$^+$ (apoptotic) cells. $n = 4$ mice per group. Data are displayed as means ± SD. Unpaired Student's two-tailed t test (B, D, I, and J). Two-way ANOVA with multiple comparisons test (G). $^{**}P < 0.01$ and $^{****}P < 0.0001$. Data are representative of three independent experiments.

E and F). Our findings revealed that Kupffer cells were the primary liver macrophage population responsible for engulfing neutrophils under steady-state conditions. However, during chronic liver injury, the absolute count of neutrophil-engulfing KCs remained unchanged despite an increase in infiltrating neutrophils. Instead, during chronic liver injury, the absolute count of neutrophil-engulfing Ly6c^{lo} and Ly6c^{hi} MoDMs was significantly increased compared to the steady state. The abundance of engulfing Ly6c^{hi} MoDMs in the fibrotic liver was comparable to that of KCs (Fig. 4G). We also observed the existence of ingested Ly6g^{+} cellular debris in all three liver macrophage populations isolated from fibrotic liver, which confirmed that the neutrophils were taken up by liver macrophages in vivo (fig. S3G).

Consistent with the hypothesis that Piezo1 knockout in macrophage impairs efferocytosis, we found that the TUNEL^{+} (terminal deoxynucleotidyl transferase–mediated deoxyuridine triphosphate nick end labeling–positive) apoptotic cells were significantly increased in Piezo1$^{fl/fl}$ Lyz2^{Cre} mice (Fig. 4, H and I). Neutrophils represent only a small part of apoptotic cells during chronic liver injury (Fig. 4J), suggesting that apoptotic neutrophils were not the only dying cells cleared by macrophages. Hepatocyte death is prominent in liver fibrosis (*22*). Immunofluorescent staining of hepatocyte nuclear factor 4 alpha (HNF4A) revealed less HNF4A-positive debris inside macrophages in Piezo1$^{fl/fl}$ Lyz2^{Cre} mice compared to WT mice, indicating impaired clearance of dead hepatocytes in macrophages lacking PIEZO1 (fig. S3H). Overall, these data demonstrated a pivotal role for Piezo1 in regulating macrophage efferocytosis in the context of tissue fibrosis.

Stiffness sensing promotes macrophage efferocytosis via Piezo1 in vitro

To determine whether Piezo1 is essential for efferocytosis, we cocultured primary mouse BMDMs from Piezo1$^{fl/fl}$ Lyz2^{Cre} mice or their littermate controls with labeled freshly isolated bone marrow neutrophils or induced apoptotic neutrophils. As expected, Piezo1-deficient BMDMs showed a decreased efferocytosis, whereas BMDMs from Piezo1$^{fl/fl}$ Lyz2^{Cre} mice and Piezo1$^{fl/fl}$ mice both showed a low-level uptake of fresh neutrophils (Fig. 5, A and B). In addition, we found that BMDMs from Piezo1$^{fl/fl}$ Lyz2^{Cre} mice were usually smaller than BMDMs from Piezo1$^{fl/fl}$ mice (Fig. 5C), attributed to the deficiency of Piezo1 impairing the calcium influx and downstream cytoskeletal organization in BMDMs (*16*, *23*). Both extracellular calcium and intracellular calcium are essential for efferocytosis (*24*, *25*). To investigate whether Piezo1 activation affects calcium influx during efferocytosis, we used live-cell imaging techniques to visualize calcium signals in BMDMs labeled with Fluo-8 during efferocytosis. Our observations revealed that, compared to fresh neutrophils, BMDMs exhibited more frequent calcium influx events when incubated with apoptotic neutrophils (Fig. 5D and movie S1). WT BMDMs cocultured with fresh or apoptotic neutrophils only uptake apoptotic neutrophils in the presence of extracellular Ca^{2+} in the medium (Fig. 5E), which suggested that calcium signaling is indispensable for efferocytosis. Using live-cell imaging, we also found that Piezo1 deficiency in BMDMs greatly reduced the frequency of calcium influx in BMDMs during efferocytosis (Fig. 5F and movie S2). Consistently, Piezo1 activation induced by Piezo1-specific agonist Yoda1 significantly increased efferocytosis in BMDMs from Piezo1$^{fl/fl}$ mice but not from Piezo1$^{fl/fl}$ Lyz2^{Cre} mice (Fig. 5G). Similar results were obtained using flow cytometry to detect efferocytosis after coculture BMDMs with apoptotic neutrophils or hepa1–6 labeled with carboxyfluorescein diacetate succinimidyl ester (CFSE) or pHrodo Deep Red (Fig. 5, H and I, and fig. S4, A and B). Treatment with cytochalasin D, a potent phagocytosis inhibitor that interferes with actin polymerization, almost completely blocked phagocytosis. After cytochalasin D treatment, we found that the binding of BMDM to apoptotic neutrophils or hepa1–6 cells was comparable (fig. S4, C and D). Piezo1 deficiency did not affect the expression of known receptors that are responsible for efferocytosis (fig. S4E). It has been reported that Piezo1 activation modulates cytoskeleton rearrangement via Rac1 (*23*). Rac1 is a small GTPase that can be activated by calcium and is crucial for phagocytosis (*26*, *27*). Immunofluorescent staining of active Rac1 showed stronger activation of Rac1 in WT macrophages during phagocytosis (Fig. 5, J and K). Together, these studies demonstrated that the Piezo1-mediated calcium signaling and Rac1 activation in macrophages are essential for efferocytosis.

Piezo1 is activated by various types of distinct mechanical stimulations, and previous studies suggested that the activation of Piezo1 can be modulated by substrate stiffness (*23*, *28*–*30*). Normal liver tissue has been reported to have an elastic modulus around several kilo Pascal, whereas fibrosis causes increased tissue rigidity to up to 20 kPa (Fig. 5L) (*31*, *32*). We hypothesized that Piezo1 could sense the increased tissue stiffness in the fibrotic liver and promote efferocytosis by macrophages during chronic liver injury. It is worth noting that the plastic plate or cover glass commonly used for macrophage culture is much stiffer (hundreds of times) compared to natural biological tissue. To better mimic the in vivo microenvironment, we measured the efferocytosis ability of BMDMs seeded on different stiffness culture matrices (0.2, 0.5, 2, 8, 16, 32, 64 kPa). We found that the uptake of apoptotic neutrophils by BMDMs increased with increased substrate stiffness (Fig. 5M). However, Piezo1-deficient BMDMs did not show an enhanced engulfment and maintained a low efferocytosis level on the stiffer matrix (Fig. 5N), suggesting that stiffness-mediated efferocytosis of neutrophils by macrophages is dependent on Piezo1. We also assessed whether increased substrate stiffness could enhance the phagocytosis activity of macrophages using fluorescent polystyrene beads (1-μm diameter). We found that the phagocytosis of beads was increased on the stiffer matrix both in WT and Piezo1-deficient BMDMs. However, Piezo1-deficient BMDMs showed less phagocytosis activity than WT BMDMs (fig. S4, F and G). Together, these data suggest that the efferocytosis by macrophages is enhanced by a stiffer substrate, which relies on the activation of Piezo1. The above results also explain why Piezo1 conditional knockout in myeloid cells only exacerbates liver inflammation and fibrosis in chronic liver injury.

Stiffness sensing and efferocytosis reprogram macrophages into an anti-inflammatory phenotype

To assess the overall effect of Piezo1 knockout on liver macrophages during chronic liver injury, three populations of liver macrophages, including KCs, Ly6c^{lo} MoDMs, and Ly6c^{hi} MoDMs from the fibrotic liver of Piezo1$^{fl/fl}$ Lyz2^{Cre} mice and Piezo1$^{fl/fl}$ mice were sorted and subjected to RNA sequencing (RNA-seq) analysis. Principal components analysis (PCA) analysis revealed a clear separation among three liver macrophage populations. Piezo1-deficient macrophages were separated from their counterparts, especially in

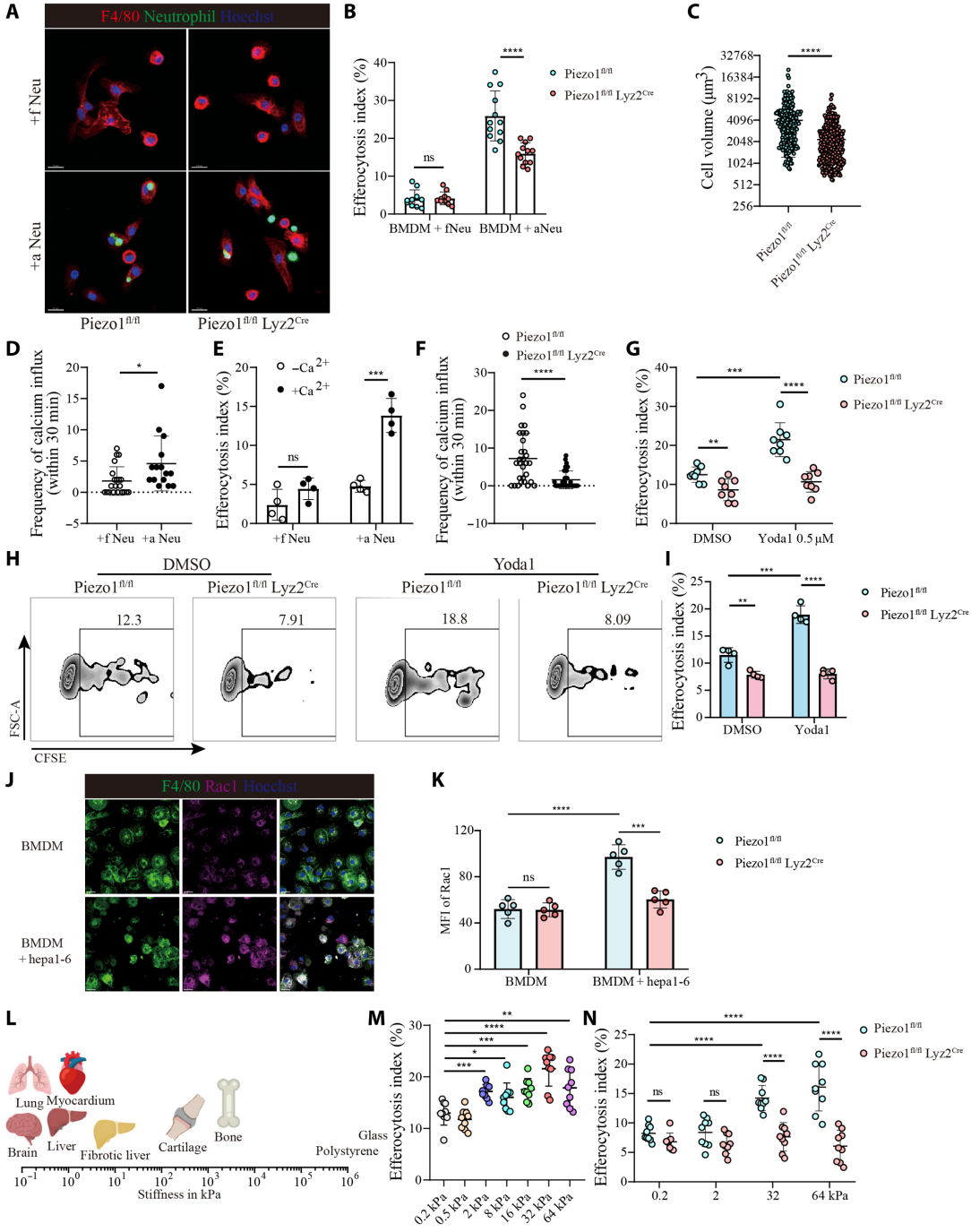

Fig. 5. Stiffness sensing promotes efferocytosis via piezo1 in vitro. (**A**) Representative confocal image of macrophages engulfing neutrophils. BMDMs (F4/80, red) were cocultured with CFSE-labeled fresh or apoptotic neutrophils (green) for 30 min. The nucleus was stained with Hoechst (blue). Scale bars, 15 μm. (**B**) Quantification of efferocytosis in experiments in (A). Each dot represents one ROI. (**C**) Quantification of cell volumes of BMDMs from indicated groups. Each dot represents one ROI. (**D**) Frequency of calcium influx in BMDMs cocultured with freshly isolated neutrophils or apoptotic neutrophils. Each spot represents an individual cell. (**E**) Efferocytosis of BMDM with or without calcium ion. Each spot represents an individual ROI. (**F**) Frequency of calcium influx in BMDMs from indicated mice cocultured with apoptotic neutrophils. Each spot represents an individual cell. (**G**) Efferocytosis of BMDMs with or without Yoda1 treatment. Each spot represents an individual ROI. (**H** and **I**) Representative FACS plot and quantifications of efferocytosis of BMDM from indicated mice, the cells were pregated from $Ly6g^{-}$ $F4/80^{+}$ population. $n = 4$ mice per group. (**J** and **K**) Active Rac1 staining (purple) in macrophages (green) with and without coculture with apoptotic hepa1–6 cells. Data are quantified as the mean fluorescent intensity of Rac1 staining in (K). Scale bars, 15 μm. $n = 5$ mice per group. (**L**) Stiffness of different tissues and plastic or glass surfaces. (**M**) Efferocytosis of BMDMs cultured in substrates with different stiffness. Each spot represents an individual ROI. (**N**) Efferocytosis of BMDMs from indicated mice cocultured with carboxyfluorescein diacetate succinimidyl ester (CFSE)–labeled apoptotic neutrophils for 30 min in substrates with different stiffness. Each spot represents an individual ROI. Data are displayed as means ± SD. One-way (M) or two-way ANOVA with multiple comparisons test (B, E, G, I, K, and N). Unpaired Student's two-tailed *t* test (C, D, and F). $*P < 0.05$, $**P < 0.01$, $***P < 0.001$, and $****P < 0.0001$. Data are representative of three independent experiments.

Ly6c^{hi} MoDMs (Fig. 6A). GO annotation showed that up-regulated genes in Piezo1-deficient Ly6c^{hi} MoDMs were related to an ECM organization, positive regulation of cell migration, inflammatory response, positive regulation of the apoptotic process, and neutrophil degranulation (Fig. 6B). Further analysis also revealed that genes related to chemotaxis, pro-inflammatory macrophage, and ECM were up-regulated in Piezo1-deficient Ly6c^{hi} MoDMs. In contrast, growth factors and anti-inflammatory macrophage-related genes were mostly down-regulated (Fig. 6C). Moreover, recent studies have identified a previously unidentified recruited liver macrophage subset as "lipid-associated macrophages" (LAMs) in mouse and human NASH, which has been shown to protect against adverse liver remodeling (*33*), and more LAM signature genes were enriched in WT but not Piezo1-deficient Ly6c^{hi}MoDMs (Fig. 6C). Analysis of KCs and Ly6c^{lo} MoDMs revealed similar changes (fig. S5, A to D). These results provided compelling evidence of the anti-inflammatory and anti-fibrosis role of Piezo1 in liver macrophage during fibrosis.

To validate these findings, we incubated CFSE-labeled human apoptotic HL-60 cells with BMDMs from Piezo1$^{fl/fl}$ Lyz2^{Cre} mice and Piezo1$^{fl/fl}$ mice, the HL-60 engulfing BMDMs were purified for qPCR. This approach allows the assessment of macrophage gene expression after efferocytosis while excluding the contamination of RNA form engulfed apoptotic cargo (*34*). To mimic stiffness-dependent efferocytosis in liver fibrosis in vitro, BMDMs were cultured on a matrix with a stiffness of 32 kPa (Fig. 6D). We observed the up-regulation of Tgfb1 and Mmp12 in Piezo1-deficient BMDMs after engulfing HL-60 (Fig. 6E). Besides, the expression of Ccl2, Ccl7, Cxcl1, Cxcl2, Cd14, Fcgr2b, and Il1b was up-regulated in lipopolysaccharide-primed BMDMs. As expected, we found that Piezo1 deficiency further increased their expressions (Fig. 6, F to M), while the expressions of Hgf and Marco were down-regulated (Fig. 6, N and O). These data are consistent with our sequencing data, suggesting that Piezo1-mediated efferocytosis reprograms macrophages into an anti-inflammatory phenotype.

Phagosome acidification in macrophages after efferocytosis requires Piezo1

The last step of efferocytosis involves the digestion of the cellular corpse. Previous studies revealed that metabolic substrates (including fatty acids and amino acids like arginine and ornithine) derived from apoptotic cells could fuel nutrient requirements for continual efferocytosis and macrophage polarization (*35*, *36*). The fact that the Piezo1-deficient macrophages failed to express anti-inflammatory genes even after engulfing apoptotic cells prompted us to investigate whether Piezo1 might also be involved in the last step of digestion. A recent study revealed that the acidification and maturation of apoptotic cells containing phagosome require calcium signaling after efferocytosis. Abrogation of calcium-conducting ion channel TRPM7 in macrophages leads to impaired acidification and digestion of phagosomal cargo (*37*). Thus, Piezo1 might also participate in the digestion of apoptotic cells and further regulate anti-inflammatory response in efferocytic macrophages.

To validate our assumption, we first evaluated the subcellular localization of Piezo1 in macrophages during efferocytosis. BMDMs from Piezo1^{P1tdT} transgenic mice were incubated with apoptotic HL-60 cells, murine neutrophils, or fluorescent polystyrene particles. To visualize the localization of Piezo1, tdTomato was labeled by anti–red fluorescent protein (RFP). We observed that Piezo1 was localized around the phagosomes containing apoptotic cells. However, this was not observed around phagosomes containing polystyrene particles (fig. S6).

Next, we used the pH-sensitive dye LysoTracker to evaluate the acidification of phagosomes after efferocytosis. Apoptotic HL-60 cells were labeled with CFSE and added to BMDMs from Piezo1$^{fl/fl}$ Lyz2^{Cre} mice or Piezo1$^{fl/fl}$ mice with or without Yoda1 for 30, 60, and 90 min. The cells were then fixed and imaged using confocal microscopy after LysoTracker staining. We observed a gradual increase in the MFI of LysoTracker in efferocytic BMDMs within 90 min, which reflected the phagosome acidification process after efferocytosis. This process was abolished by Piezo1 knockout in BMDMs. Meanwhile, Yoda1 treatment accelerated the acidification process in BMDMs from Piezo1$^{fl/fl}$ mice but not in BMDMs from Piezo1$^{fl/fl}$ Lyz2^{Cre} mice (Fig. 7, A and B). Collectively, these findings suggest that Piezo1 is required for phagosome acidification and apoptotic cargo digestion after efferocytosis, which could sustain the anti-inflammatory response of efferocytic macrophages.

Administration of Piezo1 agonist Yoda1 ameliorates liver fibrosis

We next sought to evaluate whether the global Piezo1 activation by Yoda1 could potentially serve as a therapeutic approach for treating liver fibrosis (Fig. 8A). Compared with dimethyl sulfoxide (DMSO) vehicle treatment, intraperitoneal Yoda1 administration markedly ameliorated liver fibrosis (Fig. 8, B to E). Meanwhile, neutrophil infiltration assessed by immunofluorescent staining showed a significant decrease after Yoda1 administration (Fig. 8, F and G). Flow cytometry revealed that the proportion and absolute count of neutrophils decreased after Yoda1 administration (Fig. 8, H to J), whereas liver macrophage proportions were unaffected (fig. S7A). We used flow cytometry to measure intracellular Ly6g^{+} content inside macrophages and we found increased Ly6g-positive staining in MoDMs (Fig. 8, K and L). Immunofluorescent staining of HNF4a also revealed increased HNF4a debris inside macrophages after Yoda1 treatment (fig. S7B). TUNEL staining of liver sections suggested that Yoda1 administration reduced the abundance of apoptotic cells during chronic liver injury (Fig. 8, M and N). Consistently, mRNA levels of fibrosis-related genes measured by qPCR showed a significant decrease (Fig. 8O). Serum ALT and AST levels were also decreased after Yoda1 administration (Fig. 8, P and Q). Similarly, Yoda1 administration also ameliorated liver fibrosis in the CDAHFD-induced liver fibrotic model, as revealed by decreased ALT and AST levels (Fig. 9, A and B), less Sirius red–positive staining (Fig. 9, C and D), decreased mRNA levels of fibrosis-related genes (Fig. 9E), less neutrophil infiltration, and more neutrophil efferocytosis in macrophages (Fig. 9, F to I). These results emphasized that Piezo1 might be a promising target for the clinical treatment of liver fibrosis.

DISCUSSION

Liver fibrosis is characterized by the accumulation of ECM, leading to changes in the mechanical and architectural properties of the liver (*38*). However, there is currently limited knowledge regarding how macrophages respond to these biophysical alterations and the underlying mechanisms involved. In this study, we demonstrated that macrophage Piezo1 played an important protective role in liver fibrosis. The local rigid microenvironment can activate Piezo1 in macrophages, and Piezo1 activation promotes efferocytosis

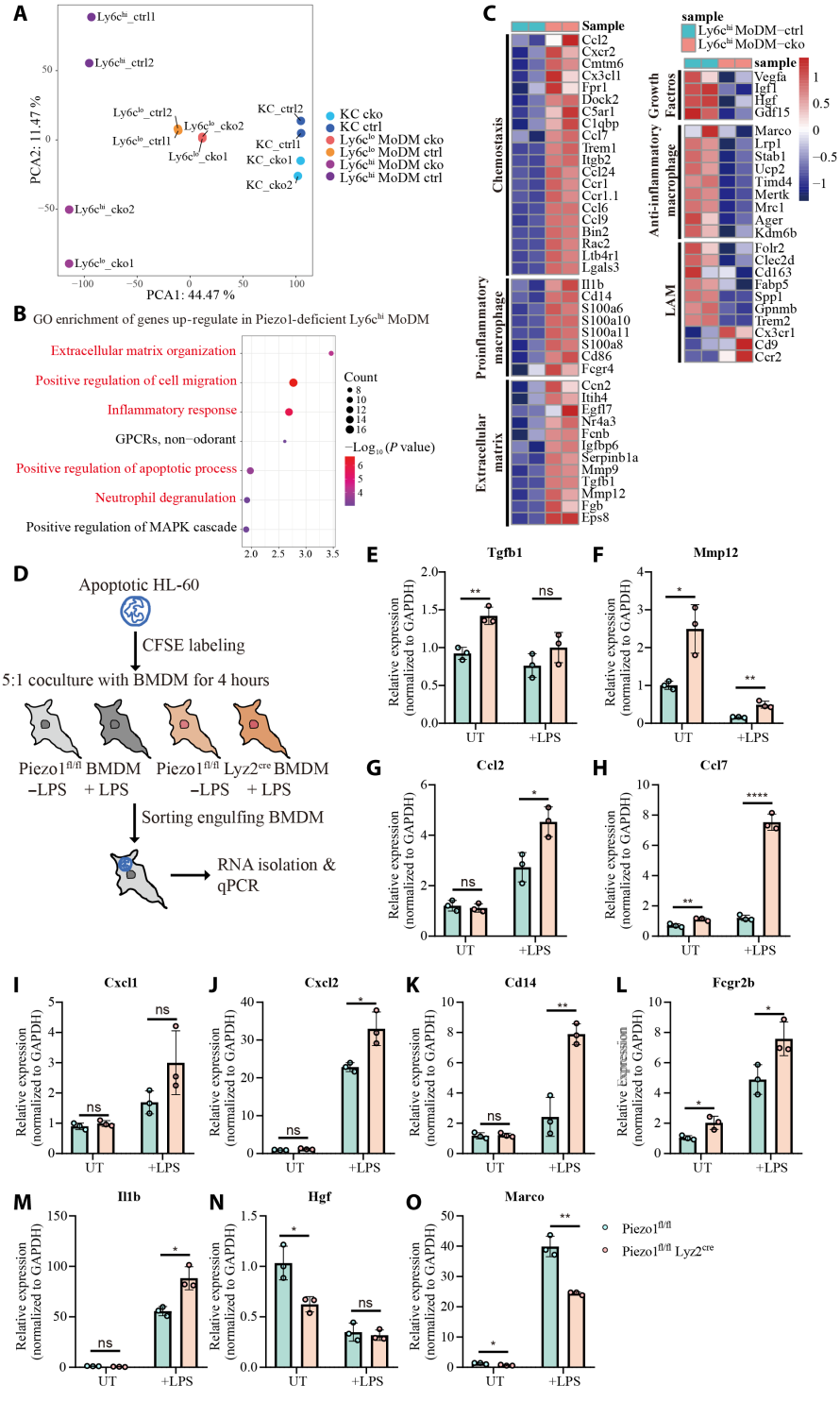

Fig. 6. Stiffness sensing and efferocytosis reprogram macrophages into an anti-inflammatory phenotype. (**A**) Principal components analysis (PCA) of bulk RNA-seq data for KCs, Ly6c^{lo} MoDMs, and Ly6c^{hi} MoDMs sorted from fibrotic liver of Piezo1$^{fl/fl}$ Lyz2^{Cre} (cko) mice and Piezo1$^{fl/fl}$ (ctrl) mice. (**B**) GO enrichment analysis of genes up-regulated in Ly6c^{hi} MoDMs from Piezo1$^{fl/fl}$ Lyz2^{Cre} mice. Pathways mentioned in the text are highlighted. (**C**) Heatmaps of differentially expressed genes (DEGs) related to chemotaxis, pro-inflammatory macrophage, ECM, growth factors, anti-inflammatory macrophage, and lipid-associated macrophage (LAM) in Ly6c^{hi} MoDMs from Piezo1$^{fl/fl}$ Lyz2^{Cre} (cko) and littermate control (ctrl). (**D**) Experimental design of efferocytosis assay using BMDMs from Piezo1$^{fl/fl}$ Lyz2^{Cre} mice and their littermate controls with or without LPS stimulation (0.1 μg/ml) cocultured with CFSE-labeled apoptotic HL-60. The engulfing BMDMs (CFSE^{+} and F4/80^{+}) were sorted for subsequent gene expression analysis. (**E** to **O**) qPCR analysis of the expression of the specified genes in efferocytic BMDMs from Piezo1$^{fl/fl}$ Lyz2^{Cre} mice and their littermate controls with or without LPS stimulation. $n = 3$ mice per group. Data are displayed as means ± SD. Unpaired Student's two-tailed t test (E to O). *$P < 0.05$, **$P < 0.01$, and ****$P < 0.0001$. Data are representative of two independent experiments.

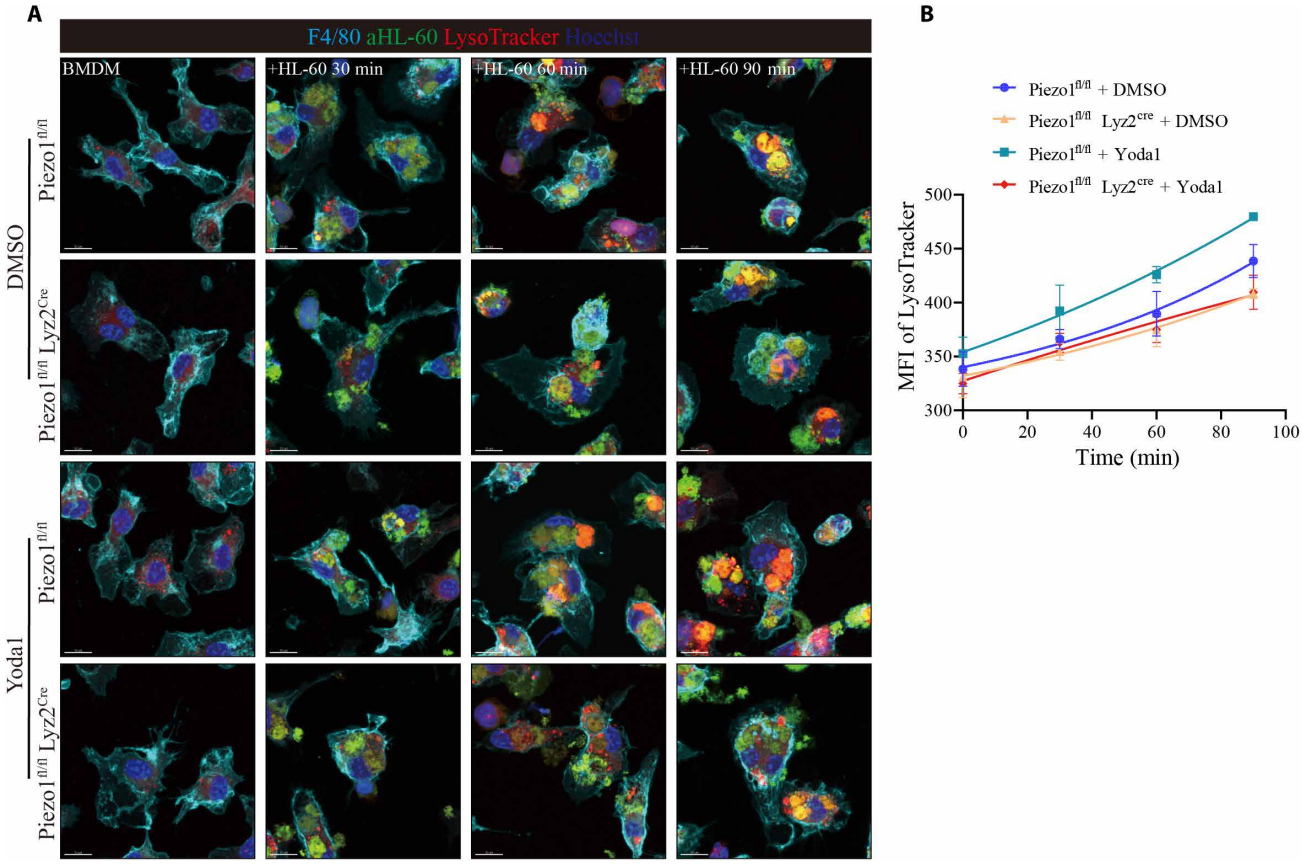

Fig. 7. Phagosome acidification in macrophages after efferocytosis requires Piezo1. (**A**) Representative confocal image showing phagosome acidification in macrophages after efferocytosis. BMDMs (visualized by F4/80, cyan) from Piezo1$^{fl/fl}$ Lyz2^{Cre} mice and their littermate controls were cocultured with CFSE-labeled apoptotic HL-60 cells (green) for 30, 60, or 90 min. The nucleus was stained with Hoechst (blue), and phagosome acidification was indicated by LysoTracker Deep Red (red). Scale bars, 10 μm. (**B**) Quantification of the MFI of LysoTracker in efferocytic BMDMs. Data are displayed as means ± SD. Data are representative of two independent experiments.

and clearance of apoptotic cells, thus limiting the pro-inflammatory response.

Macrophages exhibit high plasticity and actively adapt to mechanically distinct microenvironments (*39*). Two previous studies have suggested a crucial role of Piezo1 in pulmonary and renal fibrotic models (*13*, *14*). In both cases, piezo1 was activated by cyclic force and up-regulated the expression of pro-inflammatory genes. Activation of piezo1 in these macrophages resulted in more monocyte recruitment and exacerbated inflammation. In vitro macrophages exposed to cyclic force or cultured on rigid substrates produce higher levels of pro-inflammatory cytokines driven by Piezo1 activation (*13*, *30*). Therefore, activation of Piezo1 alone promotes the pro-inflammatory response in macrophages, although the downstream signal pathways have not been fully identified. However, these in vitro systems cannot fully recapitulate the complexity of the in vivo microenvironment. Macrophages are widely acknowledged to be major phagocytes that clear cellular debris and apoptotic neutrophils during inflammation. Here, we directly evaluated the role of Piezo1 in macrophages in a hepatic fibrosis mouse model and substantiated that the absence of Piezo1 in macrophages exacerbated fibrosis and inflammatory response. The heterogeneous roles of Piezo1 in different fibrosis models reflect the context-dependent mechanism of action; in our case, the outcome of Piezo1 activation was determined by both the type of mechanical force and the neighboring cells (apoptotic cells). Other than neutrophils, hepatocyte death is also prevalent in chronic liver disease {Lu, 2023 #50}. Our data suggested that the clearance of both hepatocytes and neutrophils was impaired in the absence of Piezo1. Therefore, Piezo1 on macrophages might be a promising target to treat hepatic fibrosis.

Defective efferocytosis has been linked to fibrotic disorders. A previous study on the effect of strain differences in fibrosis susceptibility identified the phagocytic function of macrophages as one determinant of the different outcomes in various mouse strains (*40*). Impaired macrophage phagocytosis has been reported in cirrhotic patients with ascites (*41*). Phagocytosis of apoptotic cells or liposome particles allows Ly6c^{hi} MoMCs to switch to Ly6c^{lo} macrophages, which shows a matrix-degrading phenotype and accelerates fibrosis resolution. Similarly, after bleomycin treatment, the instillation of apoptotic cells has been shown to attenuate lung injury and fibrosis through enhanced production of hepatocyte growth factor (*42*). However, it is worth mentioning that enhanced efferocytosis has been linked to pro-fibrogenesis effects. It has also been shown that efferocytosis of apoptotic alveolar epithelial cells could initiate lung fibrosis (*43*). Macrophage efferocytosis can induce the production of transforming growth factor–β (TGF-β), a well-established profibrotic cytokine. We speculate that the outcome of efferocytosis

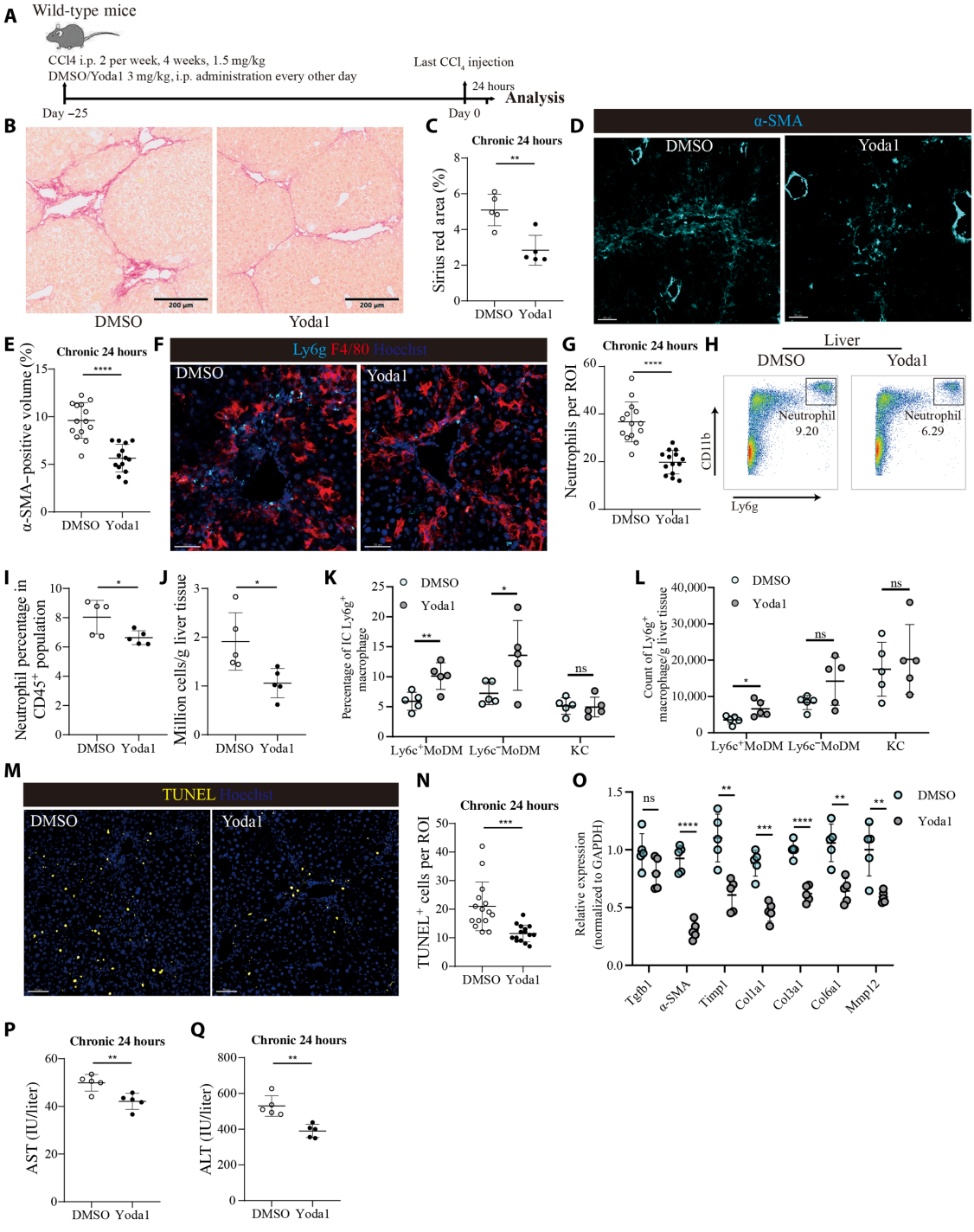

Fig. 8. Yoda1 administration ameliorates liver injury and fibrosis in the CCl_4 model. (**A**) Experimental design. (**B** and **C**) Representative image of Sirius red staining of the liver sections (B) and their quantifications (C) of dimethyl sulfoxide (DMSO) vehicle treatment and Yoda1 treatment mice 24 hours after the last CCl_4 injection. Scale bars, 200 μm. $n = 5$ mice per group. (**D** and **E**) Representative immunofluorescence staining image of α-SMA of the liver sections (D) and their quantifications (E). Scale bars, 50 μm. Each dot represents one ROI. (**F** and **G**) Representative confocal image of immunofluorescence staining of neutrophils (Ly6g, cyan) in liver sections (F) and their quantifications (G). Liver macrophages were visualized by F4/80 (red), and the nucleus was stained by Hoechst (blue). Scale bars, 50 μm. (**H** to **J**) Representative FACS plot of neutrophils (H) and statistics of their frequencies (I) and absolute count (J) in the liver. $n = 5$ mice per group. (**K** and **L**) Flow cytometry analysis of the frequency and absolute count of neutrophil-engulfing macrophages in the liver. $n = 5$ mice per group. (**M** and **N**) Representative confocal image of TUNEL (yellow) staining of liver sections (M) and their quantifications (N). Each dot represents one ROI. Scale bars, 70 μm. (**O**) qPCR analysis of mRNA level of fibrosis-related genes in the fibrotic liver. $n = 5$ mice per group. (**P** and **Q**) Quantification of serum ALT (P) and AST (Q) levels. $n = 5$ mice per group. Data are displayed as means ± SD. Unpaired Student's two-tailed t test (C, E, G, I, J, N, P, and Q). Two-way ANOVA with multiple comparisons test (K, L, and O). $^*P < 0.05$, $^{**}P < 0.01$, $^{***}P < 0.001$, and $^{****}P < 0.0001$. Data are representative of three independent experiments.

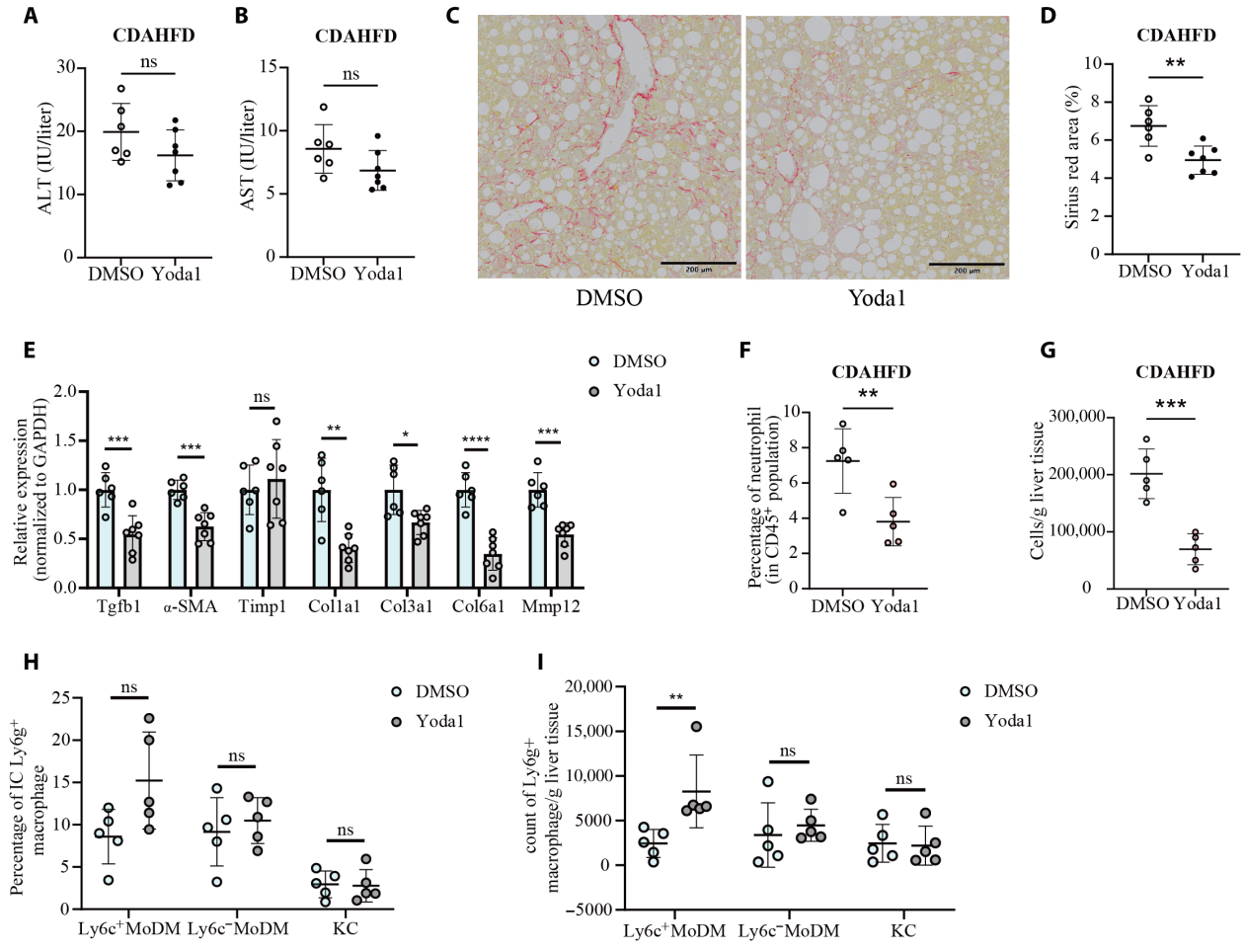

Fig. 9. Yoda1 administration ameliorates liver injury and fibrosis in the CDAHFD model. (**A** and **B**) Quantification of serum ALT (A) and AST (B) levels of control mice (DMSO) and Yoda1 treated mice (Yoda1) fed with CDAHFD diet for 6 weeks. $n = 6$ or 7 mice per group. (**C** and **D**) Representative Sirius red staining of the liver sections (C) and their quantifications (D) in control mice (DMSO) and Yoda1 treated mice (Yoda1) fed with HFCDAA diet for 6 weeks. Scale bars, 200 mm. $n = 6$ or 7 mice per group. (**E**) qPCR analysis of mRNA level of fibrosis-related genes in the liver from indicated mice. $n = 6$ or 7 mice per group. (**F** and **G**) Frequency (F) and total cell count (G) of neutrophils in liver from indicated mice. $n = 5$ mice per group. (**H** and **I**) Frequency (H) and total cell count (I) of intracellular $Ly6g^+$ macrophages in the liver from indicated mice. $n = 5$ mice per group. Data are displayed as means ± SD. Unpaired Student's two-tailed *t* test (A, B, D, and F to I). Two-way ANOVA with multiple comparisons test (E). $^*P < 0.05$, $^{**}P < 0.01$, $^{***}P < 0.001$, and $^{****}P < 0.0001$. Data are representative of two independent experiments.

by macrophages in fibrosis depends on the tissue location and the disease stages.

Although Piezo1 can promote phagocytosis through modulating cytoskeleton rearrangement via Rac1, Piezo1 itself does not serve as a scavenger receptor. Several specific receptors responsible for efferocytosis in chronic liver injury have been studied. In chronic CCl_4 liver injury, the absence of stabilin-1, the receptor responsible for taking up fibrogenic-oxidized lipids, aggravates fibrosis and delays resolution after the termination of CCl_4 (*44*). Tim4 works synergistically with TAM (Tyro3-Axl-MerTK) receptors to elicit efferocytosis, and the absence of Tim4 leads to increased inflammation and severe steatosis in both high-fat diet and methionine-choline–deficient diet-induced liver injury. Other non-TAM receptors, such as integrins avb3 and avb5, have also been shown to contribute to limiting fibrosis and the inhibition of pro-inflammatory cytokine production in the chronic liver disease models of bile duct ligation and thioacetamide-induced fibrosis (*45*). Further research is essential to investigate whether Piezo1 may affect the expression or function of these receptors.

In summary, the present study suggests that Piezo1 plays a key role in the resolution of inflammation in hepatic fibrosis. Furthermore, our study provides insights that pharmacologically targeting Piezo1 may be a promising strategy for treating liver fibrosis and immune-related diseases.

MATERIALS AND METHODS

Animals

All mice were generated on a C57BL/6 background. $Lyz2^{cre}$, $Piezo1^{P1tdT}$, and $Piezo1^{fl/fl}$ mouse strains were obtained from The Jackson Laboratory (Jackson Laboratories stock nos. 004781, 029214, and 029213, respectively). $Piezo1^{fl/fl}$ mice were crossed with $Lyz2^{cre}$ mice to generate $Piezo1^{fl/fl}$ $Lyz2^{cre}$ mice. Only littermate mice were used when comparing WT and Piezo1 knockout. Sex-matched 7- to 10-week-old mice were used to induce liver injury and fibrosis, CCl_4 was

1:9 dissolved in corn oil, and CCl_4 (1.5 g/kg) was injected intraperitoneally twice a week for over 4 weeks (*46*). Mice on CDAHFD were started at 8 weeks of age and were maintained on the same diet for 6 weeks. For Yoda1 treatment, Yoda1 was given every other day during the CCl_4 treatment or CDAHFD diet. All animals were maintained at 12-hour light/dark cycles under controlled temperature and humidity conditions. All animal experiments were performed in compliance with the animal center of Shanghai Jiao Tong University School of Medicine.

Cell isolation and culture

For BMDM, bone marrow cells were collected by flushing the femurs and tibias with phosphate-buffered saline (PBS) in a 1-ml sterile syringe. After red blood cell lysis by ACK (Gibco A1049201), 1×10^7 bone marrow cells were plated in 10-cm dish and cultured in Dulbecco's modified Eagle's medium (Gibco) supplemented with 2 mM L-glutamine, 10% heat-inactivated fetal bovine serum (FBS) (Gibco), 1% penicillin/streptomycin (absin), and recombinant mouse macrophage colony-stimulating factor (20 ng/ml; PeproTech, 315-02). The culture medium was replaced on day 3, and the cells were allowed to differentiate for 7 days. For neutrophils, bone marrow cells after erythrocyte lysis were resuspended in Hanks' balanced salt solution (HBSS) (Gibco) supplemented with 20 mM Na-Hepes (Solarbio, H1095) and 0.5% FBS, layered on 62.5% Percoll gradient (Cytiva, 17089109) and centrifuged at 1000*g* for 30 min with no break. Neutrophils were collected after discarding the upper layer and washed for further experiment. To induce apoptosis, purified neutrophils were incubated in RPMI 1640 medium (Gibco) without FBS for 24 hours (*47*). The apoptotic rate was confirmed to be >80% with annexin V and propidium iodide staining (Yeasen, 40305BS20). HL-60 cell line was cultured in Iscove's modified Dulbecco's medium (Gibco, C12440500BT) supplemented with 2 mM L-glutamine, 15% heat-inactivated FBS, and 1% penicillin/streptomycin. Paclitaxel (0.1 nM; Selleckchem, S1150) was added to induce apoptosis; the apoptotic rate was greater than 90% after 48 hours of paclitaxel treatment.

Efferocytosis assay

BMDMs were harvested using PBS (HyClone) supplemented 2 mM EDTA (Invitrogen AM9260G) and seeded at a 5×10^4 cells/cm^2 density 24 hours before the experiment. For experiments on stiffness culture matrix (Sigma-Aldrich, 5190-7EA), the matrix surfaces were coated with collagen I (50 μg/ml) from rat tail (Corning, 354236) before seeding. For some experiments, BMDM was treated with LPS (0.1 μg/ml; Sigma-Aldrich, L2630) for 24 hours. Apoptotic cells were labeled with 5 μM CFSE (eBioscience, 65-0850-84) or pHrodo Deep Red (Invitrogen, P35357), followed by the manufacturer's instructions. The apoptotic cells were then cocultured with BMDMs in a 5:1 ratio to BMDMs for 30 min (unless otherwise indicated). Cells were washed three times with PBS and fixed with 4% paraformaldehyde (PFA; Servicebio, G1101) at room temperature for 15 min. To assess phagosome acidification, the cells were stained with 50 nM LysoTracker Red (Invitrogen, L7528) at room temperature for 30 min in PBS before fixation. The cells were then permeabilized with 0.2% Triton X-100 dissolved in PBS at room temperature for 15 min and followed by PE-F4/80 (BioLegend, 123110) antibody staining overnight at 4°C and Hoechst (Invitrogen H1399) staining for 15 min at room temperature. Phagocytosis was then assessed by confocal imaging. For flow cytometry, the cells were harvested after washing with PBS and stained with PE-F4/80 and Pacific Blue Ly6g (BioLegend, 127611) before flow cytometry acquisition performed on BD LSRFortessa X-20 (BD Biosciences) using FACSDiva software.

Live-cell imaging

BMDMs were harvested and then labeled with 0.5 μM CellTracker CMRA (Invitrogen, C34551), and apoptotic neutrophils or fresh neutrophils were labeled with 0.25 μM CellTracker Deep Red (Invitrogen, C34565), and then washed twice after incubating 30 min. Labeled BMDMs were then seeded into a confocal dish for 1 hour, 3 μM Fluo-8 (Abcam, ab142773), and Deep Red–labeled neutrophils were added and incubated for 30 min. Time-lapse imaging was then performed by an inverted Olympus FV3000 confocal microscope with a 20×/0.75 UPLANSAPO objective lens; images were taken every 20 s for 30 min.

Mice treatment and sampling

Yoda1 was purchased from MCE (HY-18723) and was dissolved into 10 mg/ml stock in DMSO. In some experiments, after being dissolved in a 1:9 ratio with corn oil, Yoda1 (3 mg/kg) was given intraperitoneally every other day during the CCl_4 challenge. The control mice were given an equivalent amount of DMSO dissolved in corn oil. The mice were anesthetized with 2.5% Avertin (20 ml/kg) and sampled 24 or 48 hours after the last injection. Specifically, 300 μl of blood was collected first from the postcava using a 1-ml syringe and placed on ice. One hundred microliters was used for flow cytometry and 200 μl for serum collection after centrifugation (4000 rpm, 15 min) and cryopreserved at −20°C to measure ALT and AST. Then, the mice were euthanized, and the liver was perfused with 20 ml of cold PBS. The liver tissue was sampled after perfusion for subsequent assays, including flow cytometry analysis, frozen section preparation for immunofluorescence, histology examination, and RNA isolation for qRT-PCR.

Flow cytometry

Peripheral blood from mice was lysed with ACK and centrifuged at 1500 rpm for 5 min. Bone marrow cells were collected, as mentioned above. The liver was placed in RPMI 1640 complete medium supplemented with collagenase IV (0.2 mg/ml; Sigma-Aldrich, C5318) and deoxyribonuclease I (0.05 mg/ml; Sigma-Aldrich, D4513), cut into pieces, and incubated at 37°C 30 min for enzyme digest. Single-cell suspension was made after using a 1.2-mm syringe to dissociate the digested tissue. The collected cells were first stained with Zombie Aqua dye (BioLegend, 423102) to exclude dead cells. The cells were then stained with fluorophore-conjugated anti-mouse antibodies at 4°C. Antibodies used in experiments included anti-CD45 (clone 30-F11), anti-CD11b (clone M1/70), anti-CD64 (clone X54-5/7.1), anti-F4/80 (clone BM8), anti-Ly6c (clone HK1.4), anti-Ly6g (clone 1A8), anti-Siglecf (clone E50-2440), anti-CD31 (clone 390), and anti-B220 (clone RA3-6B2). For intracellular staining, cells were fixed and permeabilized using the Foxp3/Transcription Factor Staining Buffer Set (eBioscience, 00-5523-00) following the manufacturer's protocol after surface staining. Intracellular Ly6g was stained using phycoerythrin-conjugated anti-mouse Ly6g (clone 1A8) after intracellular Fc-blocking. The cells were resuspended in 200 μl of fluorescence-activated cell sorting (FACS) buffer, and counting beads (Invitrogen C36950) were added according to the manufacturer's protocol before flow cytometry acquisition. Flow cytometry acquisition was performed on BD LSRFortessa X-20 (BD

Biosciences) using FACSDiva software, and the data were analyzed by FlowJo software (Tree Star).

MACS enrichment and cell sorting

For the enrichment and sorting of liver macrophages, we used a modified protocol in which the liver was digested and dissociated by collagenase perfusion as described (*48*). Briefly, the liver was digested by perfused with 37°C prewarmed 15 ml of HBSS containing 0.5 mM EDTA and 10 ml of HBSS containing 1 mM $CaCl_2$ and collagenase (6.4 mg/ml) (Sigma-Aldrich, C9407) via the vena cava and hepatic portal vein. Then, the liver was collected, and hepatic cells were released by removing the liver capsule and cutting the liver lobes. The cells were then filtered through a 100-μm cell strainer. Liver macrophages in the supernatant were then enriched by magnetic-activated cell sorting (MACS) before sorting. The cells were incubated with biotinylated anti-mouse F4/80 (1:100; clone BM8) antibody followed by streptavidin microbeads (1:10; Miltenyi Biotec, 130-048-101). Liver macrophages were positively selected using LS columns and a MidiMACS separator (Miltenyi Biotec) according to the manufacturer's instructions. Selected cells were next stained with fluorophore-conjugated anti-mouse antibodies, including anti-CD45 (clone 30-F11), anti-CD11b (clone M1/70), anti-CD64 (clone X54-5/7.1), anti-F4/80 (clone BM8), anti-Ly6c (clone HK1.4), anti-Ly6g (clone 1A8), anti-Siglecf (clone E50-2440), anti-CD31 (clone 390), anti-B220 (clone RA3-6B2) after dead cell staining and Fc blocking. All antibodies are from BioLegend. Cell sorting was performed on a BD FACSAria III (BD Biosciences) instrument to achieve >98% purity and >85% viability.

Immunofluorescence

The liver samples were fixed using 4% PFA overnight. Samples were embedded in an OCT compound (Sakura Finetek) and stored at −80°C. Frozen sections of 50 μm thickness were cut on a CM1950 cryostat (Leica), followed by permeabilization with PBS containing 0.2% Triton X-100 and blocking with PBS containing 0.2% Tween 20, 1% bovine serum albumin, 0.3 M glycine, and 10% goat serum for 2 hours at room temperature. The sections were stained with primary antibodies, including anti-Ly6g (clone 1A8, BioLegend), anti-F4/80 (clone BM8, BioLegend), anti–α-SMA (clone EPR4429, Abcam), and anti-HNF4A (SN72-03, Thermo Fisher Scientific) diluted using PBS containing 0.2% Tween 20 followed by Goat anti-Rabbit secondary antibody (Jackson Immunoresearch, 111-605-003) and Hoechst staining for 2 hours. In some experiments, primary antibodies, including anti-RFP (clone EPR18992, Abcam), anti-Ly6c (clone HK1.4, BioLegend), and anti-Timd4 (clone RMT4-54, BioLegend), were used. For TUNEL staining of the liver section, the TUNEL Apoptosis Detection Kit (Alexa Fluor 640, Yeasen 40308ES20) was used following the manufacturer's protocol.

Confocal microscopy and image processing

The image acquisition was performed on an FV3000 confocal microscope with 20×/0.75 UPLANSAPO or 60×/1.30 Sil UPLANSAPO objective lens. Laser excitation wavelengths of 405, 488, 561, and 647 nm were used for fluorescence detection. A mosaic image of the liver section was acquired using a 4 × 4 field of view, and three regions of interest (ROIs) were selected for analysis. Images were processed using Imaris (Bitplane) and Fiji (NIH) software. A background subtraction algorithm determined the threshold, and neutrophil number and α-SMA–positive volume were quantified using the spot and surface functions in Imaris. Histo-cytometry analysis was performed to quantify tdTomato fluorescence intensity as previously described (*49*). Briefly, surfaces of liver macrophages were created according to F4/80 staining, and the MFI for all channels was obtained using Imaris. Objects were exported into FlowJo 10.3 and later analyzed with GraphPad Prism. To quantify efferocytosis, images were acquired with a 10×/0.40 UPLANSAPO objective lens, zoom ×3. The efferocytosis index was evaluated as the percentage of engulfing BMDMs in at least three fields per sample.

Histology

Liver samples were embedded in paraffin, and 10-μm-thick sections were obtained after fixation and dehydration. Dewaxed paraffin sections were stained with Sirius red solution (Servicebio, G1018) for 8 min, and then dehydrated thrice with anhydrous ethanol. The sections were then sealed with neutral gum (SCRC 10004160) after hyalinized with xylene. The images were acquired using an FV200 microscopy system with a 40× objective lens. The percentage of Sirius red–positive area was evaluated using Fiji software.

Biochemical assay

The serum ALT and AST levels were measured using the Alanine Aminotransferase Assay Kit and Aspartate Aminotransferase Assay Kit (Nanjing Jiancheng Bioengineering Institute, C009-2-1 and C010-2-1, respectively) following the manufacturer's protocol.

Quantitative real-time PCR

Total RNA was extracted using TRIzol reagent (Invitrogen, 15596018), and cDNA was synthesized by reverse transcription using HiScript II Q RT SuperMix (Vazyme, R223-01) according to the manufacturer's instructions. Gene expression was quantified using AceQ Universal SYBR qPCR Master Mix (Vazyme, Q511-02). Primers used to detect mouse genes are listed in table S1.

RNA sequencing

The total RNA of the isolated liver macrophage was extracted as described above. Quality control of extracted RNA was performed using Agilent 4200 Bioanalyzer (Agilent Technologies, Santa Clara, CA, USA). The libraries were constructed using VAHTS Universal V6 RNA-Seq Library Prep Kit (Vazyme, NR604-01) according to the manufacturer's instructions and sequenced using the Illumina Novoseq 6000 platform (Novogene). About 50 M of 150–base pair paired-end reads per sample were generated on average. After the removal of low-quality reads, filtered clean reads were mapped to the reference genome using HISAT2. FPKM (fragments per kilobase per million mapped reads) of each gene was then calculated, and the corresponding read counts were obtained by HTSeq-count.

Bioinformatics analysis

For the analysis of public repositories of human and mice transcription profiling datasets, processed data were downloaded from Array Express (https://www.ebi.ac.uk/biostudies/arrayexpress/studies) and NCBI Gene Expression Omnibus (www.ncbi.nlm.nih.gov/geo/) and processed using R (www.r-project.org/) and Prism. The top 100 genes positively or negatively correlated with PIEZO1 in the human transcription profiling dataset were calculated using R and were used for subsequent biological function analysis using Metascape (*50*). For the analysis of RNA-seq data, differential gene expression was analyzed using DeSeq2 (*51*), and significantly differentially

expressed genes (DEGs) were determined by $Q < 0.05$ and $0.5 < \log_2$ (fold change) < -0.5. Biofunction analysis was performed using these DEGs with EnrichR (*52*). Volcano plot, PCA plot, and bar plots were generated using ggplot2. Heatmaps were generated using pheatmap.

Statistical analysis

Unless otherwise specified, all experiments were performed two or three times independently. Representative images of immunofluorescence staining, Sirius red staining, and flow cytometry plots are shown. Statistical analyses were performed using GraphPad Prism software. All data replicates indicated represent the mean values ± SDs. Statistical significance was determined using unpaired Student's two-tailed *t* test for comparisons between two groups, and one-way analysis of variance (ANOVA) with Tukey's multiple comparisons test or two-way ANOVA with Sidak's multiple comparisons test for comparisons between multiple groups or repeated measures.

Supplementary Materials

This PDF file includes:

Figs. S1 to S7
Table S1
Legends for movies S1 and S2

Other Supplementary Material for this manuscript includes the following:

Movies S1 and S2

REFERENCES AND NOTES

1. T. Kisseleva, D. Brenner, Molecular and cellular mechanisms of liver fibrosis and its regression. *Nat. Rev. Gastroenterol. Hepatol.* **18**, 151–166 (2021).
2. S. Mueller, L. Sandrin, Liver stiffness: A novel parameter for the diagnosis of liver disease. *Hepat. Med.* **2**, 49–67 (2010).
3. A. L. Olsen, S. A. Bloomer, E. P. Chan, M. D. A. Gaça, P. C. Georges, B. Sackey, M. Uemura, P. A. Janmey, R. G. Wells, Hepatic stellate cells require a stiff environment for myofibroblastic differentiation. *Am. J. Physiol. Gastrointest. Liver Physiol.* **301**, G110–G118 (2011).
4. L. Liu, Z. You, H. Yu, L. Zhou, H. Zhao, X. Yan, D. Li, B. Wang, L. Zhu, Y. Xu, T. Xia, Y. Shi, C. Huang, W. Hou, Y. Du, Mechanotransduction-modulated fibrotic microniches reveal the contribution of angiogenesis in liver fibrosis. *Nat. Mater.* **16**, 1252–1261 (2017).
5. P. Ramachandran, J. P. Iredale, Macrophages: Central regulators of hepatic fibrogenesis and fibrosis resolution. *J. Hepatol.* **56**, 1417–1419 (2012).
6. P. Ramachandran, A. Pellicoro, M. A. Vernon, L. Boulter, R. L. Aucott, A. Ali, S. N. Hartland, V. K. Snowdon, A. Cappon, T. T. Gordon-Walker, M. J. Williams, D. R. Dunbar, J. R. Manning, N. van Rooijen, J. A. Fallowfield, S. J. Forbes, J. P. Iredale, Differential Ly-6C expression identifies the recruited macrophage phenotype, which orchestrates the regression of murine liver fibrosis. *Proc. Natl. Acad. Sci. U.S.A.* **109**, E3186–E3195 (2012).
7. J. S. Duffield, S. J. Forbes, C. M. Constandinou, S. Clay, M. Partolina, S. Vuthoori, S. Wu, R. Lang, J. P. Iredale, Selective depletion of macrophages reveals distinct, opposing roles during liver injury and repair. *J. Clin. Invest.* **115**, 56–65 (2005).
8. Y. Wen, J. Lambrecht, C. Ju, F. Tacke, Hepatic macrophages in liver homeostasis and diseases-diversity, plasticity and therapeutic opportunities. *Cell. Mol. Immunol.* **18**, 45–56 (2021).
9. D. T. Reid, J. L. Reyes, B. A. McDonald, T. Vo, R. A. Reimer, B. Eksteen, Kupffer cells undergo fundamental changes during the development of experimental NASH and are critical in initiating liver damage and inflammation. *PLOS ONE* **11**, e0159524 (2016).
10. M. Chen, Y. Zhang, P. Zhou, X. Liu, H. Zhao, X. Zhou, Q. Gu, B. Li, X. Zhu, Q. Shi, Substrate stiffness modulates bone marrow-derived macrophage polarization through NF-κB signaling pathway. *Bioact. Mater.* **5**, 880–890 (2020).
11. X. Xing, Y. Wang, X. Zhang, X. Gao, M. Li, S. Wu, Y. Zhao, J. Chen, D. Gao, R. Chen, Z. Ren, K. Zhang, J. Cui, Matrix stiffness-mediated effects on macrophages polarization and their LOXL2 expression. *FEBS J.* **288**, 3465–3477 (2021).
12. S. E. Murthy, A. E. Dubin, A. Patapoutian, Piezos thrive under pressure: Mechanically activated ion channels in health and disease. *Nat. Rev. Mol. Cell Biol.* **18**, 771–783 (2017).
13. A. G. Solis, P. Bielecki, H. R. Steach, L. Sharma, C. C. D. Harman, S. Yun, M. R. de Zoete, J. N. Warnock, S. D. F. To, A. G. York, M. Mack, M. A. Schwartz, C. S. dela Cruz, N. W. Palm, R. Jackson, R. A. Flavell, Mechanosensation of cyclical force by PIEZO1 is essential for innate immunity. *Nature* **573**, 69–74 (2019).
14. Y. He, B. Deng, S. Liu, S. Luo, Y. Ning, X. Pan, R. Wan, Y. Chen, Z. Zhang, J. Jiang, H. Xu, M. Xia, J. Li, Myeloid piezo1 deletion protects renal fibrosis by restraining macrophage infiltration and activation. *Hypertension* **79**, 918–931 (2022).
15. L. Hoyles, J. M. Fernández-Real, M. Federici, M. Serino, J. Abbott, J. Charpentier, C. Heymes, J. L. Luque, E. Anthony, R. H. Barton, J. Chilloux, A. Myridakis, L. Martinez-Gili, J. M. Moreno-Navarrete, F. Benhamed, V. Azalbert, V. Blasco-Baque, J. Puig, G. Xifra, W. Ricart, C. Tomlinson, M. Woodbridge, M. Cardellini, F. Davato, I. Cardolini, O. Porzio, P. Gentileschi, F. Lopez, F. Foufelle, S. A. Butcher, E. Holmes, J. K. Nicholson, C. Postic, R. Burcelin, M. E. Dumas, Molecular phenomics and metagenomics of hepatic steatosis in non-diabetic obese women. *Nat. Med.* **24**, 1070–1080 (2018).
16. S. Ma, A. E. Dubin, Y. Zhang, S. A. R. Mousavi, Y. Wang, A. M. Coombs, M. Loud, I. Andolfo, A. Patapoutian, A role of PIEZO1 in iron metabolism in mice and humans. *Cell* **184**, 969–982.e13 (2021).
17. J. S. Seidman, T. D. Troutman, M. Sakai, A. Gola, N. J. Spann, H. Bennett, C. M. Bruni, Z. Ouyang, R. Z. Li, X. Sun, B. C. T. Vu, M. P. Pasillas, K. M. Ego, D. Gosselin, V. M. Link, L. W. Chong, R. M. Evans, B. M. Thompson, J. G. McDonald, M. Hosseini, J. L. Witztum, R. N. Germain, C. K. Glass, Niche-specific reprogramming of epigenetic landscapes drives myeloid cell diversity in nonalcoholic steatohepatitis. *Immunity* **52**, 1057–1074.e7 (2020).
18. M. Matsumoto, N. Hada, Y. Sakamaki, A. Uno, T. Shiga, C. Tanaka, T. Ito, A. Katsume, M. Sudoh, An improved mouse model that rapidly develops fibrosis in non-alcoholic steatohepatitis. *Int. J. Exp. Pathol.* **94**, 93–103 (2013).
19. J. Shi, G. E. Gilbert, Y. Kokubo, T. Ohashi, Role of the liver in regulating numbers of circulating neutrophils. *Blood* **98**, 1226–1230 (2001).
20. C. Hong, Y. Kidani, N. A-Gonzalez, T. Phung, A. Ito, X. Rong, K. Ericson, H. Mikkola, S. W. Beaven, L. S. Miller, W. H. Shao, P. L. Cohen, A. Castrillo, P. Tontonoz, S. J. Bensinger, Coordinate regulation of neutrophil homeostasis by liver X receptors in mice. *J. Clin. Invest.* **122**, 337–347 (2012).
21. T. N. Bukong, Y. Cho, A. Iracheta-Vellve, B. Saha, P. Lowe, A. Adejumo, I. Furi, A. Ambade, B. Gyongyosi, D. Catalano, K. Kodys, G. Szabo, Abnormal neutrophil traps and impaired efferocytosis contribute to liver injury and sepsis severity after binge alcohol use. *J. Hepatol.* **69**, 1145–1154 (2018).
22. J. L. Lu, C. X. Yu, L. J. Song, Programmed cell death in hepatic fibrosis: Current and perspectives. *Cell Death Discov.* **9**, 449 (2023).
23. J. Geng, Y. Shi, J. Zhang, B. Yang, P. Wang, W. Yuan, H. Zhao, J. Li, F. Qin, L. Hong, C. Xie, X. Deng, Y. Sun, C. Wu, L. Chen, D. Zhou, TLR4 signalling via Piezo1 engages and enhances the macrophage mediated host response during bacterial infection. *Nat. Commun.* **12**, 3519 (2021).
24. L. Cuttell, A. Vaughan, E. Silva, C. J. Escaron, M. Lavine, E. van Goethem, J. P. Eid, M. Quirin, N. C. Franc, Undertaker, a Drosophila Junctophilin, links Draper-mediated phagocytosis and calcium homeostasis. *Cell* **135**, 524–534 (2008).
25. M. A. Gronski, J. M. Kinchen, I. J. Juncadella, N. C. Franc, K. S. Ravichandran, An essential role for calcium flux in phagocytes for apoptotic cell engulfment and the anti-inflammatory response. *Cell Death Differ.* **16**, 1323–1331 (2009).
26. Y. Mao, S. C. Finnemann, Regulation of phagocytosis by Rho GTPases. *Small GTPases* **6**, 89–99 (2015).
27. J. M. Cook-Mills, J. D. Johnson, T. L. Deem, A. Ochi, L. Wang, Y. Zheng, Calcium mobilization and Rac1 activation are required for VCAM-1 (vascular cell adhesion molecule-1) stimulation of NADPH oxidase activity. *Biochem. J.* **378**, 539–547 (2004).
28. M. M. Pathak, J. L. Nourse, T. Tran, J. Hwe, J. Arulmoli, D. T. T. Ie, E. Bernardis, L. A. Flanagan, F. Tombola, Stretch-activated ion channel Piezo1 directs lineage choice in human neural stem cells. *Proc. Natl. Acad. Sci. U.S.A.* **111**, 16148–16153 (2014).
29. B. Aykut, R. Chen, J. I. Kim, D. Wu, S. A. A. Shadaloey, R. Abengozar, P. Preiss, A. Saxena, S. Pushalkar, J. Leinwand, B. Diskin, W. Wang, G. Werba, M. Berman, S. K. B. Lee, A. Khodadadi-Jamayran, D. Saxena, W. A. Coetzee, G. Miller, Targeting Piezo1 unleashes innate immunity against cancer and infectious disease. *Sci. Immunol.* **5**, eabb5168 (2020).
30. H. Atcha, A. Jairaman, J. R. Holt, V. S. Meli, R. R. Nagalla, P. K. Veerasubramanian, K. T. Brumm, H. E. Lim, S. Othy, M. D. Cahalan, M. M. Pathak, W. F. Liu, Mechanically activated ion channel Piezo1 modulates macrophage polarization and stiffness sensing. *Nat. Commun.* **12**, 3256 (2021).
31. S. Affo, L. X. Yu, R. F. Schwabe, The role of cancer-associated fibroblasts and fibrosis in liver cancer. *Annu. Rev. Pathol.* **12**, 153–186 (2017).
32. C. F. Guimarães, L. Gasperini, A. P. Marques, R. L. Reis, The stiffness of living tissues and its implications for tissue engineering. *Nat. Rev. Mater.* **5**, 351–370 (2020).
33. S. Daemen, A. Gainullina, G. Kalugotla, L. He, M. M. Chan, J. W. Beals, K. H. Liss, S. Klein, A. E. Feldstein, B. N. Finck, M. N. Artyomov, J. D. Schilling, Dynamic shifts in the composition of resident and recruited macrophages influence tissue remodeling in NASH. *Cell Rep.* **34**, 108626 (2021).
34. S. Maschalidi, P. Mehrotra, B. N. Keçeli, H. K. L. de Cleene, K. Lecomte, R. van der Cruyssen, P. Janssen, J. Pinney, G. van Loo, D. Elewaut, A. Massie, E. Hoste, K. S. Ravichandran,

Targeting SLC7A11 improves efferocytosis by dendritic cells and wound healing in diabetes. *Nature* **606**, 776–784 (2022).
35. S. Zhang, S. Weinberg, M. DeBerge, A. Gainullina, M. Schipma, J. M. Kinchen, I. Ben-Sahra, D. R. Gius, L. Yvan-Charvet, N. S. Chandel, P. T. Schumacker, E. B. Thorp, Efferocytosis fuels requirements of fatty acid oxidation and the electron transport chain to polarize macrophages for tissue repair. *Cell Metab.* **29**, 443–456.e5 (2019).
36. A. Yurdagul Jr., M. Subramanian, X. Wang, S. B. Crown, O. R. Ilkayeva, L. Darville, G. K. Kolluru, C. C. Rymond, B. D. Gerlach, Z. Zheng, G. Kuriakose, C. G. Kevil, J. M. Koomen, J. L. Cleveland, D. M. Muoio, I. Tabas, Macrophage metabolism of apoptotic cell-derived arginine promotes continual efferocytosis and resolution of injury. *Cell Metab.* **31**, 518–533.e10 (2020).
37. M. S. Schappe, M. E. Stremska, G. W. Busey, T. K. Downs, P. V. Seegren, S. K. Mendu, Z. Flegal, C. A. Doyle, E. J. Stipes, B. N. Desai, Efferocytosis requires periphagosomal Ca^{2+}-signaling and TRPM7-mediated electrical activity. *Nat. Commun.* **13**, 3230 (2022).
38. J. Herrera, C. A. Henke, P. B. Bitterman, Extracellular matrix as a driver of progressive fibrosis. *J. Clin. Invest.* **128**, 45–53 (2018).
39. N. Jain, J. Moeller, V. Vogel, Mechanobiology of macrophages: How physical factors coregulate macrophage plasticity and phagocytosis. *Annu. Rev. Biomed. Eng.* **21**, 267–297 (2019).
40. P. An, L. L. Wei, S. Zhao, D. Y. Sverdlov, K. A. Vaid, M. Miyamoto, K. Kuramitsu, M. Lai, Y. V. Popov, Hepatocyte mitochondria-derived danger signals directly activate hepatic stellate cells and drive progression of liver fibrosis. *Nat. Commun.* **11**, 2362 (2020).
41. A. M. M. Ahmed, A. Bomford, K. T. Nouri-Aria, T. Davies, R. Smith, R. Williams, Peritoneal macrophages from patients with cirrhotic ascites show impaired phagocytosis and vigorous respiratory burst. *Results Immunol.* **1**, 53–59 (2011).
42. Y. J. Lee, C. Moon, S. H. Lee, H. J. Park, J. Y. Seoh, M. S. Cho, J. L. Kang, Apoptotic cell instillation after bleomycin attenuates lung injury through hepatocyte growth factor induction. *Eur. Respir. J.* **40**, 424–435 (2012).
43. K. K. Kim, M. R. Dotson, M. Agarwal, J. Yang, P. B. Bradley, N. Subbotina, J. J. Osterholzer, T. H. Sisson, Efferocytosis of apoptotic alveolar epithelial cells is sufficient to initiate lung fibrosis. *Cell Death Dis.* **9**, 1056 (2018).
44. P. Rantakari, D. A. Patten, J. Valtonen, M. Karikoski, H. Gerke, H. Dawes, J. Laurila, S. Ohlmeier, K. Elima, S. G. Hübscher, C. J. Weston, S. Jalkanen, D. H. Adams, M. Salmi, S. Shetty, Stabilin-1 expression defines a subset of macrophages that mediate tissue homeostasis and prevent fibrosis in chronic liver injury. *Proc. Natl. Acad. Sci. U.S.A.* **113**, 9298–9303 (2016).
45. E. Patsenker, Y. Popov, F. Stickel, V. Schneider, M. Ledermann, H. Sägesser, G. Niedobitek, S. L. Goodman, D. Schuppan, Pharmacological inhibition of integrin alphavbeta3 aggravates experimental liver fibrosis and suppresses hepatic angiogenesis. *Hepatology* **50**, 1501–1511 (2009).
46. B. S. Ding, Z. Cao, R. Lis, D. J. Nolan, P. Guo, M. Simons, M. E. Penfold, K. Shido, S. Y. Rabbany, S. Rafii, Divergent angiocrine signals from vascular niche balance liver regeneration and fibrosis. *Nature* **505**, 97–102 (2014).
47. I. Kourtzelis, X. Li, I. Mitroulis, D. Grosser, T. Kajikawa, B. Wang, M. Grzybek, J. von Renesse, A. Czogalla, M. Troullinaki, A. Ferreira, C. Doreth, K. Ruppova, L. S. Chen, K. Hosur, J. H. Lim, K. J. Chung, S. Grosskklaus, A. K. Tausche, L. A. B. Joosten, N. M. Moutsopoulos, B. Wielockx, A. Castrillo, J. M. Korostoff, Ü. Coskun, G. Hajishengallis, T. Chavakis, DEL-1 promotes macrophage efferocytosis and clearance of inflammation. *Nat. Immunol.* **20**, 40–49 (2019).
48. M. Aparicio-Vergara, M. Tencerova, C. Morgantini, E. Barreby, M. Aouadi, Isolation of Kupffer cells and hepatocytes from a single mouse liver. *Methods Mol. Biol.* **1639**, 161–171 (2017).
49. M. Y. Gerner, W. Kastenmuller, I. Ifrim, J. Kabat, R. N. Germain, Histo-cytometry: A method for highly multiplex quantitative tissue imaging analysis applied to dendritic cell subset microanatomy in lymph nodes. *Immunity* **37**, 364–376 (2012).
50. Y. Zhou, B. Zhou, L. Pache, M. Chang, A. H. Khodabakhshi, O. Tanaseichuk, C. Benner, S. K. Chanda, Metascape provides a biologist-oriented resource for the analysis of systems-level datasets. *Nat. Commun.* **10**, 1523 (2019).
51. M. I. Love, W. Huber, S. Anders, Moderated estimation of fold change and dispersion for RNA-seq data with DESeq2. *Genome Biol.* **15**, 550 (2014).
52. E. Y. Chen, C. M. Tan, Y. Kou, Q. Duan, Z. Wang, G. V. Meirelles, N. R. Clark, A. Ma'ayan, Enrichr: Interactive and collaborative HTML5 gene list enrichment analysis tool. *BMC Bioinformatics* **14**, 128 (2013).

Acknowledgments: We thank the Core Facility of Shanghai Institute of Immunology, Shanghai Jiao Tong University School of Medicine for technical help with flow cytometry and immunofluorescence microscopy. We thank the Home for Researchers editorial team (www.home-for-researchers.com) for the language editing service. **Funding:** This work was supported by grants from The Ministry of Science and Technology of China (2020YFC2002800 to Jing Wang), the National Natural Science Foundation of China (82371760,81822020, 92042304, 31872737 to Jing Wang; and 82302069 to Yina Wang). **Author contributions:** Conceptualization: Jing Wang. Methodology: Jin Wang, Yang Wang, and J.Z. Investigation: Jin Wang, Yang Wang, J.Z., Yina Wang, Yuanyuan Wang, H.K., W.Z., W.B., and N.M. Visualization: Yang Wang, J.Z., and Jing Wang. Supervision: Jing Wang. Writing—original draft: Yang Wang and Jing Wang. Writing—review and editing: Jing Wang. **Competing interests:** The authors declare that they have no competing interests. **Data and materials availability:** All data needed to evaluate the conclusions in the paper are present in the paper and/or the Supplementary Materials. The RNA sequencing data have been deposited in the Gene Expression Omnibus (GEO) of NCBI under the accession number PRJNA978380.

Submitted 20 June 2023
Accepted 1 May 2024
Published 5 June 2024
10.1126/sciadv.adj3289